Measurement of the b-hadron Production Cross Section Using Decays to $\mu^- D^0 X$ Final States in $p\bar{p}$ Collisions at $\sqrt{s} = 1.96\,\mathrm{TeV}$

T. Aaltonen,[24] J. Adelman,[14] T. Akimoto,[56] B. Álvarez González[s],[12] S. Amerio[y],[44] D. Amidei,[35] A. Anastassov,[39] A. Annovi,[20] J. Antos,[15] G. Apollinari,[18] A. Apresyan,[49] T. Arisawa,[58] A. Artikov,[16] W. Ashmanskas,[18] A. Attal,[4] A. Aurisano,[54] F. Azfar,[43] W. Badgett,[18] A. Barbaro-Galtieri,[29] V.E. Barnes,[49] B.A. Barnett,[26] P. Barria[aa],[47] V. Bartsch,[31] G. Bauer,[33] P.-H. Beauchemin,[34] F. Bedeschi,[47] D. Beecher,[31] S. Behari,[26] G. Bellettini[z],[47] J. Bellinger,[60] D. Benjamin,[17] A. Beretvas,[18] J. Beringer,[29] A. Bhatti,[51] M. Binkley,[18] D. Bisello[y],[44] I. Bizjak[ee],[31] R.E. Blair,[2] C. Blocker,[7] B. Blumenfeld,[26] A. Bocci,[17] A. Bodek,[50] V. Boisvert,[50] G. Bolla,[49] D. Bortoletto,[49] J. Boudreau,[48] A. Boveia,[11] B. Brau[a],[11] A. Bridgeman,[25] L. Brigliadori[x],[6] C. Bromberg,[36] E. Brubaker,[14] J. Budagov,[16] H.S. Budd,[50] S. Budd,[25] S. Burke,[18] K. Burkett,[18] G. Busetto[y],[44] P. Bussey,[22] A. Buzatu,[34] K. L. Byrum,[2] S. Cabrera[u],[17] C. Calancha,[32] M. Campanelli,[36] M. Campbell,[35] F. Canelli[14],[18] A. Canepa,[46] B. Carls,[25] D. Carlsmith,[60] R. Carosi,[47] S. Carrillo[n],[19] S. Carron,[34] B. Casal,[12] M. Casarsa,[18] A. Castro[x],[6] P. Catastini[aa],[47] D. Cauz[dd],[55] V. Cavaliere[aa],[47] M. Cavalli-Sforza,[4] A. Cerri,[29] L. Cerrito[o],[31] S.H. Chang,[28] Y.C. Chen,[1] M. Chertok,[8] G. Chiarelli,[47] G. Chlachidze,[18] F. Chlebana,[18] K. Cho,[28] D. Chokheli,[16] J.P. Chou,[23] G. Choudalakis,[33] S.H. Chuang,[53] K. Chung,[13] W.H. Chung,[60] Y.S. Chung,[50] T. Chwalek,[27] C.I. Ciobanu,[45] M.A. Ciocci[aa],[47] A. Clark,[21] D. Clark,[7] G. Compostella,[44] M.E. Convery,[18] J. Conway,[8] M. Cordelli,[20] G. Cortiana[y],[44] C.A. Cox,[8] D.J. Cox,[8] F. Crescioli[z],[47] C. Cuenca Almenar[u],[8] J. Cuevas[s],[12] R. Culbertson,[18] J.C. Cully,[35] D. Dagenhart,[18] M. Datta,[18] T. Davies,[22] P. de Barbaro,[50] S. De Cecco,[52] A. Deisher,[29] G. De Lorenzo,[4] M. Dell'Orso[z],[47] C. Deluca,[4] L. Demortier,[51] J. Deng,[17] M. Deninno,[6] P.F. Derwent,[18] A. Di Canto[z],[47] G.P. di Giovanni,[45] C. Dionisi[cc],[52] B. Di Ruzza[dd],[55] J.R. Dittmann,[5] M. D'Onofrio,[4] S. Donati[z],[47] P. Dong,[9] J. Donini,[44] T. Dorigo,[44] S. Dube,[53] J. Efron,[40] A. Elagin,[54] R. Erbacher,[8] D. Errede,[25] S. Errede,[25] R. Eusebi,[18] H.C. Fang,[29] S. Farrington,[43] W.T. Fedorko,[14] R.G. Feild,[61] M. Feindt,[27] J.P. Fernandez,[32] C. Ferrazza[bb],[47] R. Field,[19] G. Flanagan,[49] R. Forrest,[8] M.J. Frank,[5] M. Franklin,[23] J.C. Freeman,[18] I. Furic,[19] M. Gallinaro,[52] J. Galyardt,[13] F. Garberson,[11] J.E. Garcia,[21] A.F. Garfinkel,[49] P. Garosi[aa],[47] K. Genser,[18] H. Gerberich,[25] D. Gerdes,[35] A. Gessler,[27] S. Giagu[cc],[52] V. Giakoumopoulou,[3] P. Giannetti,[47] K. Gibson,[48] J.L. Gimmell,[50] C.M. Ginsburg,[18] N. Giokaris,[3] M. Giordani[dd],[55] P. Giromini,[20] M. Giunta,[47] G. Giurgiu,[26] V. Glagolev,[16] D. Glenzinski,[18] M. Gold,[38] N. Goldschmidt,[19] A. Golossanov,[18] G. Gomez,[12] G. Gomez-Ceballos,[33] M. Goncharov,[33] O. González,[32] I. Gorelov,[38] A.T. Goshaw,[17] K. Goulianos,[51] A. Gresele[y],[44] S. Grinstein,[23] C. Grosso-Pilcher,[14] R.C. Group,[18] U. Grundler,[25] J. Guimaraes da Costa,[23] Z. Gunay-Unalan,[36] C. Haber,[29] K. Hahn,[33] S.R. Hahn,[18] E. Halkiadakis,[53] B.-Y. Han,[50] J.Y. Han,[50] F. Happacher,[20] K. Hara,[56] D. Hare,[53] M. Hare,[57] S. Harper,[43] R.F. Harr,[59] R.M. Harris,[18] M. Hartz,[48] K. Hatakeyama,[51] C. Hays,[43] M. Heck,[27] A. Heijboer,[46] J. Heinrich,[46] C. Henderson,[33] M. Herndon,[60] J. Heuser,[27] S. Hewamanage,[5] D. Hidas,[17] C.S. Hill[c],[11] D. Hirschbuehl,[27] A. Hocker,[18] S. Hou,[1] M. Houlden,[30] S.-C. Hsu,[29] B.T. Huffman,[43] R.E. Hughes,[40] U. Husemann,[61] M. Hussein,[36] J. Huston,[36] J. Incandela,[11] G. Introzzi,[47] M. Iori[cc],[52] A. Ivanov,[8] E. James,[18] D. Jang,[13] B. Jayatilaka,[17] E.J. Jeon,[28] M.K. Jha,[6] S. Jindariani,[18] W. Johnson,[8] M. Jones,[49] K.K. Joo,[28] S.Y. Jun,[13] J.E. Jung,[28] T.R. Junk,[18] T. Kamon,[54] D. Kar,[19] P.E. Karchin,[59] Y. Kato[l],[42] R. Kephart,[18] W. Ketchum,[14] J. Keung,[46] V. Khotilovich,[54] B. Kilminster,[18] D.H. Kim,[28] H.S. Kim,[28] H.W. Kim,[28] J.E. Kim,[28] M.J. Kim,[20] S.B. Kim,[28] S.H. Kim,[56] Y.K. Kim,[14] N. Kimura,[56] L. Kirsch,[7] S. Klimenko,[19] B. Knuteson,[33] B.R. Ko,[17] K. Kondo,[58] D.J. Kong,[28] J. Konigsberg,[19] A. Korytov,[19] A.V. Kotwal,[17] J.A. Kraus,[25] M. Kreps,[27] J. Kroll,[46] D. Krop,[14] N. Krumnack,[5] M. Kruse,[17] V. Krutelyov,[11] T. Kubo,[56] T. Kuhr,[27] N.P. Kulkarni,[59] M. Kurata,[56] S. Kwang,[14] A.T. Laasanen,[49] S. Lami,[47] S. Lammel,[18] M. Lancaster,[31] R.L. Lander,[8] K. Lannon[r],[40] A. Lath,[53] G. Latino[aa],[47] I. Lazzizzera[y],[44] T. LeCompte,[2] E. Lee,[54] H.S. Lee,[14] S.W. Lee[t],[54] S. Leone,[47] J.D. Lewis,[18] C.-S. Lin,[29] J. Linacre,[43] M. Lindgren,[18] E. Lipeles,[46] A. Lister,[8] D.O. Litvintsev,[18] C. Liu,[48] T. Liu,[18] N.S. Lockyer,[46] A. Loginov,[61] M. Loreti[y],[44] L. Lovas,[15] D. Lucchesi[y],[44] C. Luci[cc],[52] J. Lueck,[27] P. Lujan,[29] P. Lukens,[18] G. Lungu,[51] L. Lyons,[43] J. Lys,[29] R. Lysak,[15] D. MacQueen,[34] R. Madrak,[18] K. Maeshima,[18] K. Makhoul,[33] T. Maki,[24] P. Maksimovic,[26] S. Malde,[43] S. Malik,[31] G. Manca[e],[30] A. Manousakis-Katsikakis,[3] F. Margaroli,[49] C. Marino,[27] C.P. Marino,[25] A. Martin,[61] V. Martin[k],[22] M. Martínez,[4] R. Martínez-Ballarín,[32] T. Maruyama,[56] P. Mastrandrea,[52] T. Masubuchi,[56] M. Mathis,[26] M.E. Mattson,[59] P. Mazzanti,[6] K.S. McFarland,[50] P. McIntyre,[54] R. McNulty[j],[30] A. Mehta,[30] P. Mehtala,[24] A. Menzione,[47] P. Merkel,[49] C. Mesropian,[51] T. Miao,[18] N. Miladinovic,[7] R. Miller,[36] C. Mills,[23] M. Milnik,[27] A. Mitra,[1] G. Mitselmakher,[19] H. Miyake,[56] N. Moggi,[6] C.S. Moon,[28] R. Moore,[18] M.J. Morello,[47] J. Morlock,[27] P. Movilla Fernandez,[18] J. Mülmenstädt,[29] A. Mukherjee,[18] Th. Muller,[27] R. Mumford,[26] P. Murat,[18] M. Mussini[x],[6] J. Nachtman,[18] Y. Nagai,[56] A. Nagano,[56] J. Naganoma,[56]

K. Nakamura,[56] I. Nakano,[41] A. Napier,[57] V. Necula,[17] J. Nett,[60] C. Neu[v],[46] M.S. Neubauer,[25] S. Neubauer,[27]
J. Nielsen[g],[29] L. Nodulman,[2] M. Norman,[10] O. Norniella,[25] E. Nurse,[31] L. Oakes,[43] S.H. Oh,[17] Y.D. Oh,[28]
I. Oksuzian,[19] T. Okusawa,[42] R. Orava,[24] K. Osterberg,[24] S. Pagan Griso[y],[44] E. Palencia,[18] V. Papadimitriou,[18]
A. Papaikonomou,[27] A.A. Paramonov,[14] B. Parks,[40] S. Pashapour,[34] J. Patrick,[18] G. Pauletta[dd],[55] M. Paulini,[13]
C. Paus,[33] T. Peiffer,[27] D.E. Pellett,[8] A. Penzo,[55] T.J. Phillips,[17] G. Piacentino,[47] E. Pianori,[46] L. Pinera,[19]
K. Pitts,[25] C. Plager,[9] L. Pondrom,[60] O. Poukhov[*],[16] N. Pounder,[43] F. Prakoshyn,[16] A. Pronko,[18] J. Proudfoot,[2]
F. Ptohos[i],[18] E. Pueschel,[13] G. Punzi[z],[47] J. Pursley,[60] J. Rademacker[c],[43] A. Rahaman,[48] V. Ramakrishnan,[60]
N. Ranjan,[49] I. Redondo,[32] P. Renton,[43] M. Renz,[27] M. Rescigno,[52] S. Richter,[27] F. Rimondi[x],[6] L. Ristori,[47]
A. Robson,[22] T. Rodrigo,[12] T. Rodriguez,[46] E. Rogers,[25] S. Rolli,[57] R. Roser,[18] M. Rossi,[55] R. Rossin,[11]
P. Roy,[34] A. Ruiz,[12] J. Russ,[13] V. Rusu,[18] B. Rutherford,[18] H. Saarikko,[24] A. Safonov,[54] W.K. Sakumoto,[50]
O. Saltó,[4] L. Santi[dd],[55] S. Sarkar[cc],[52] L. Sartori,[47] K. Sato,[18] A. Savoy-Navarro,[45] P. Schlabach,[18] A. Schmidt,[27]
E.E. Schmidt,[18] M.A. Schmidt,[14] M.P. Schmidt[*],[61] M. Schmitt,[39] T. Schwarz,[8] L. Scodellaro,[12] A. Scribano[aa],[47]
F. Scuri,[47] A. Sedov,[49] S. Seidel,[38] Y. Seiya,[42] A. Semenov,[16] L. Sexton-Kennedy,[18] F. Sforza[z],[47] A. Sfyrla,[25]
S.Z. Shalhout,[59] T. Shears,[30] P.F. Shepard,[48] M. Shimojima[q],[56] S. Shiraishi,[14] M. Shochet,[14] Y. Shon,[60]
I. Shreyber,[37] P. Sinervo,[34] A. Sisakyan,[16] A.J. Slaughter,[18] J. Slaunwhite,[40] K. Sliwa,[57] J.R. Smith,[8] F.D. Snider,[18]
R. Snihur,[34] A. Soha,[8] S. Somalwar,[53] V. Sorin,[36] T. Spreitzer,[34] P. Squillacioti[aa],[47] M. Stanitzki,[61] R. St. Denis,[22]
B. Stelzer,[34] O. Stelzer-Chilton,[34] D. Stentz,[39] J. Strologas,[38] G.L. Strycker,[35] J.S. Suh,[28] A. Sukhanov,[19]
I. Suslov,[16] T. Suzuki,[56] A. Taffard[f],[25] R. Takashima,[41] Y. Takeuchi,[56] R. Tanaka,[41] M. Tecchio,[35] P.K. Teng,[1]
K. Terashi,[51] J. Thom[h],[18] A.S. Thompson,[22] G.A. Thompson,[25] E. Thomson,[46] P. Tipton,[61] P. Ttito-Guzmán,[32]
S. Tkaczyk,[18] D. Toback,[54] S. Tokar,[15] K. Tollefson,[36] T. Tomura,[56] D. Tonelli,[18] S. Torre,[20] D. Torretta,[18]
P. Totaro[dd],[55] S. Tourneur,[45] M. Trovato[bb],[47] S.-Y. Tsai,[1] Y. Tu,[46] N. Turini[aa],[47] F. Ukegawa,[56] S. Vallecorsa,[21]
N. van Remortel[b],[24] A. Varganov,[35] E. Vataga[bb],[47] F. Vázquez[n],[19] G. Velev,[18] C. Vellidis,[3] M. Vidal,[32] R. Vidal,[18]
I. Vila,[12] R. Vilar,[12] T. Vine,[31] M. Vogel,[38] I. Volobouev[t],[29] G. Volpi[z],[47] P. Wagner,[46] R.G. Wagner,[2]
R.L. Wagner,[18] W. Wagner[w],[27] J. Wagner-Kuhr,[27] T. Wakisaka,[42] R. Wallny,[9] S.M. Wang,[1] A. Warburton,[34]
D. Waters,[31] M. Weinberger,[54] J. Weinelt,[27] W.C. Wester III,[18] B. Whitehouse,[57] D. Whiteson[f],[46] A.B. Wicklund,[2]
E. Wicklund,[18] S. Wilbur,[14] G. Williams,[34] H.H. Williams,[46] P. Wilson,[18] B.L. Winer,[40] P. Wittich[h],[18]
S. Wolbers,[18] C. Wolfe,[14] T. Wright,[35] X. Wu,[21] F. Würthwein,[10] S. Xie,[33] A. Yagil,[10] K. Yamamoto,[42]
J. Yamaoka,[17] U.K. Yang[p],[14] Y.C. Yang,[28] W.M. Yao,[29] G.P. Yeh,[18] J. Yoh,[18] K. Yorita,[58] T. Yoshida[m],[42]
G.B. Yu,[50] I. Yu,[28] S.S. Yu,[18] J.C. Yun,[18] L. Zanello[cc],[52] A. Zanetti,[55] X. Zhang,[25] Y. Zheng[d],[9] and S. Zucchelli[x],[6]

(CDF Collaboration[†])

[1]*Institute of Physics, Academia Sinica, Taipei, Taiwan 11529, Republic of China*
[2]*Argonne National Laboratory, Argonne, Illinois 60439*
[3]*University of Athens, 157 71 Athens, Greece*
[4]*Institut de Fisica d'Altes Energies, Universitat Autonoma de Barcelona, E-08193, Bellaterra (Barcelona), Spain*
[5]*Baylor University, Waco, Texas 76798*
[6]*Istituto Nazionale di Fisica Nucleare Bologna, [x]University of Bologna, I-40127 Bologna, Italy*
[7]*Brandeis University, Waltham, Massachusetts 02254*
[8]*University of California, Davis, Davis, California 95616*
[9]*University of California, Los Angeles, Los Angeles, California 90024*
[10]*University of California, San Diego, La Jolla, California 92093*
[11]*University of California, Santa Barbara, Santa Barbara, California 93106*
[12]*Instituto de Fisica de Cantabria, CSIC-University of Cantabria, 39005 Santander, Spain*
[13]*Carnegie Mellon University, Pittsburgh, PA 15213*

^{14}Enrico Fermi Institute, University of Chicago, Chicago, Illinois 60637

^{15}Comenius University, 842 48 Bratislava, Slovakia; Institute of Experimental Physics, 040 01 Kosice, Slovakia

^{16}Joint Institute for Nuclear Research, RU-141980 Dubna, Russia

^{17}Duke University, Durham, North Carolina 27708

^{18}Fermi National Accelerator Laboratory, Batavia, Illinois 60510

^{19}University of Florida, Gainesville, Florida 32611

^{20}Laboratori Nazionali di Frascati, Istituto Nazionale di Fisica Nucleare, I-00044 Frascati, Italy

^{21}University of Geneva, CH-1211 Geneva 4, Switzerland

^{22}Glasgow University, Glasgow G12 8QQ, United Kingdom

^{23}Harvard University, Cambridge, Massachusetts 02138

^{24}Division of High Energy Physics, Department of Physics,
University of Helsinki and Helsinki Institute of Physics, FIN-00014, Helsinki, Finland

^{25}University of Illinois, Urbana, Illinois 61801

^{26}The Johns Hopkins University, Baltimore, Maryland 21218

^{27}Institut für Experimentelle Kernphysik, Universität Karlsruhe, 76128 Karlsruhe, Germany

^{28}Center for High Energy Physics: Kyungpook National University,
Daegu 702-701, Korea; Seoul National University, Seoul 151-742,
Korea; Sungkyunkwan University, Suwon 440-746,
Korea; Korea Institute of Science and Technology Information, Daejeon,
305-806, Korea; Chonnam National University, Gwangju, 500-757, Korea

^{29}Ernest Orlando Lawrence Berkeley National Laboratory, Berkeley, California 94720

^{30}University of Liverpool, Liverpool L69 7ZE, United Kingdom

^{31}University College London, London WC1E 6BT, United Kingdom

^{32}Centro de Investigaciones Energeticas Medioambientales y Tecnologicas, E-28040 Madrid, Spain

^{33}Massachusetts Institute of Technology, Cambridge, Massachusetts 02139

^{34}Institute of Particle Physics: McGill University, Montréal, Québec,
Canada H3A 2T8; Simon Fraser University, Burnaby, British Columbia,
Canada V5A 1S6; University of Toronto, Toronto, Ontario,
Canada M5S 1A7; and TRIUMF, Vancouver, British Columbia, Canada V6T 2A3

^{35}University of Michigan, Ann Arbor, Michigan 48109

^{36}Michigan State University, East Lansing, Michigan 48824

^{37}Institution for Theoretical and Experimental Physics, ITEP, Moscow 117259, Russia

^{38}University of New Mexico, Albuquerque, New Mexico 87131

^{39}Northwestern University, Evanston, Illinois 60208

^{40}The Ohio State University, Columbus, Ohio 43210

^{41}Okayama University, Okayama 700-8530, Japan

^{42}Osaka City University, Osaka 588, Japan

^{43}University of Oxford, Oxford OX1 3RH, United Kingdom

^{44}Istituto Nazionale di Fisica Nucleare, Sezione di Padova-Trento, ^{y}University of Padova, I-35131 Padova, Italy

^{45}LPNHE, Universite Pierre et Marie Curie/IN2P3-CNRS, UMR7585, Paris, F-75252 France

^{46}University of Pennsylvania, Philadelphia, Pennsylvania 19104

^{47}Istituto Nazionale di Fisica Nucleare Pisa, ^{z}University of Pisa,
^{aa}University of Siena and ^{bb}Scuola Normale Superiore, I-56127 Pisa, Italy

^{48}University of Pittsburgh, Pittsburgh, Pennsylvania 15260

^{49}Purdue University, West Lafayette, Indiana 47907

^{50}University of Rochester, Rochester, New York 14627

^{51}The Rockefeller University, New York, New York 10021

^{52}Istituto Nazionale di Fisica Nucleare, Sezione di Roma 1,
^{cc}Sapienza Università di Roma, I-00185 Roma, Italy

^{53}Rutgers University, Piscataway, New Jersey 08855

^{54}Texas A&M University, College Station, Texas 77843

^{55}Istituto Nazionale di Fisica Nucleare Trieste/Udine,
I-34100 Trieste, ^{dd}University of Trieste/Udine, I-33100 Udine, Italy

^{56}University of Tsukuba, Tsukuba, Ibaraki 305, Japan

^{57}Tufts University, Medford, Massachusetts 02155

^{58}Waseda University, Tokyo 169, Japan

^{59}Wayne State University, Detroit, Michigan 48201

^{60}University of Wisconsin, Madison, Wisconsin 53706

^{61}Yale University, New Haven, Connecticut 06520

We report a measurement of the production cross section for b hadrons in $p\bar{p}$ collisions at $\sqrt{s} = 1.96\,\mathrm{TeV}$. Using a data sample derived from an integrated luminosity $83\,\mathrm{pb}^{-1}$ collected with the upgraded Collider Detector (CDF II) at the Fermilab Tevatron, we analyze b hadrons, H_b, partially reconstructed in the semileptonic decay mode $H_b \to \mu^- D^0 X$. Our measurement of the inclusive

production cross section for b hadrons with transverse momentum $p_T > 9\,\mathrm{GeV}/c$ and rapidity $|y| < 0.6$ is $\sigma = 1.30\,\mu\mathrm{b} \pm 0.05\,\mu\mathrm{b}(\mathrm{stat}) \pm 0.14\,\mu\mathrm{b}(\mathrm{syst}) \pm 0.07\mu\mathrm{b}(\mathcal{B})$, where the uncertainties are statistical, systematic, and from branching fractions respectively. The differential cross sections $d\sigma/dp_T$ are found to be in good agreement with recent measurements of the H_b cross section and well described by fixed-order next-to-leading logarithm predictions.

PACS numbers: 14.40.Nd, 12.15.Ff, 12.15.Hh, 13.20.He

I. INTRODUCTION

Measurements of the b-hadron production cross section in high energy $p\bar{p}$ collisions provide an excellent test of perturbative quantum chromodynamics (QCD). Next-to-leading order (NLO) calculations of the b-hadron cross section [1, 2] have been available for more than a decade. These NLO calculations have been recently supplemented with corrections for terms proportional to $\alpha_s^2[\alpha_s \log(p_T/m_b)]^k$ and $\alpha_s^3[\alpha_s \log(p_T/m_b)]^k$ with $k \geq 1$, where α_s is the strong coupling constant, p_T is the transverse momentum of the b hadron, and m_b is the mass of the bottom quark. These calculations are referred to as fixed order next-to-leading logarithm (FONLL) [3].

A number of b-hadron cross section measurements have been performed at the Tevatron. In the 1992-1996 running period, Tevatron Run I, measurements were performed at $\sqrt{s} = 1.8\,\mathrm{TeV}$ by the CDF and D0 experiments using several different techniques and final states [4–7]. These measurements were consistently higher than theoretical expectations from NLO calculations.

Since 2001, the Tevatron has been running at $\sqrt{s} = 1.96\,\mathrm{TeV}$. To date, the CDF Collaboration has made two inclusive b-hadron cross section measurements at the higher center-of-mass energy. The first was an inclusive measurement using $H_b \to J/\psi X, J/\psi \to \mu^+\mu^-$ decays, where H_b denotes a b hadron [8]. This measurement was performed for $|y| < 0.6$ [9] and was the first to map out the b-hadron cross section down to zero transverse momentum. The $H_b \to J/\psi X$ cross section result, along with an improved FONLL calculation [3], prompted studies [10, 11] suggesting that prior discrepancies had been resolved with improved measurement and calculational techniques.

More recently, the CDF collaboration has performed a measurement of the B^+ meson cross section using $740\,\mathrm{pb}^{-1}$ of data through the fully reconstructed decay chain $B^+ \to J/\psi K^+$, with $J/\psi \to \mu^+\mu^-$, for B^+ transverse momentum, $p_T(B^+)$, greater than $6\,\mathrm{GeV}/c$ and $|y| < 1$. With large statistics and a high purity signal, the total uncertainty on this measurement is smaller than 10% [12]. The result is also in good agreement with FONLL calculations. The difference between the original NLO calculation and the current FONLL calculation arises from a number of different factors, as discussed in Ref. [10].

While improved theoretical calculations compare favorably to recent measurements, more experimental input is needed. In particular, cross-section measurements using different H_b decay modes can be complementary to one another since they might be acquired using different trigger paths and be subject to different background contributions. For example, Ref. [13] showed that previous b-hadron cross section measurements were inconsistent when comparing semileptonic and J/ψ final states.

In this paper, we present the first measurement of the H_b cross section using semileptonic decays at $\sqrt{s} = 1.96\,\mathrm{TeV}$. This analysis takes advantage of the distinct semileptonic b-hadron decay signature and provides a measurement that is complementary to those made in $H_b \to J/\psi X$ modes. We reconstruct signals of semileptonic b hadron decays, $H_b \to \mu^- D X$, where charm mesons, D^0 and D^{*+}, are reconstructed in fully hadronic modes, using a data sample acquired with a dedicated semileptonic trigger path. Throughout this paper, any reference to a specific charge state implies the antiparticle state as well.

Previous measurements of the b-hadron cross section at the Tevatron using semileptonic decays were performed using inclusive $H_b \to \mu^- X$ [6, 7] and the semielectronic $H_b \to e^- D^0 X$ [5] modes. There are no previously published b-hadron cross section results from the Tevatron utilizing the $H_b \to \mu^- D^0 X$ mode. We improve upon prior semileptonic results with a comparable data sample by extending the measurement to lower values of $p_T(H_b)$ than have been accessible in previous analyses. The trigger path used in this analysis, which will be described in detail below, accepts muons with $p_T > 4\,\mathrm{GeV}/c$ while previous measurements were limited to leptons with $p_T > 8\,\mathrm{GeV}/c$.

We begin in Sec. II with an overview of the measurement technique. The CDF II detector and trigger system will be described in Sec. III, followed by a discussion of trigger selection in Sec. IV. Section V will describe the event selection and candidate reconstruction. Sections VI and VII then describe the measurements of signal reconstruction efficiency and acceptance, followed by an assessment of the background contributions in Sec. VIII. In Sec. IX, we present our results along with a comparison to theoretical predictions.

II.   OVERVIEW OF THE MEASUREMENT

We select events with an identified muon in conjunction with a fully reconstructed charm meson (D^0 or D^{*+}, generically referred to as a D meson) such that the $\mu^- D$ topology is consistent with a b-hadron decay. To measure the cross section, we count the number of signal events and correct for detector acceptance, identification inefficiency, and contributions from background sources. Incorporating these factors, along with the measured $p\bar{p}$ luminosity, $\mathcal{L}$, we extract the cross section, σ, times branching ratio ($\mathcal{B}$) in the following way:

$$\sigma(p\bar{p} \to H_b X) \times \mathcal{B} = \frac{N(1 - f_{bck})}{2 \times \alpha \times \epsilon \times \mathcal{L}} \quad , \tag{1}$$

where N is the number of observed candidate $\mu^- D^0$ ($\mu^- D^{*+}$) events and f_{bck} is the background fraction, *i.e.* the fraction of events not originating from the decay of a b hadron. The acceptance α is defined as the fraction of events in which the muon and the charm decay particles pass through active regions of the CDF II detector. The detection efficiency ϵ is the fraction of these events which are reconstructed.

The product of branching ratios, $\mathcal{B}$, is shorthand for $\mathcal{B}(H_b \to \mu^- D^0 X) \times \mathcal{B}(D^0 \to K^- \pi^+)$ in the $\mu^- D^0$ mode and $\mathcal{B}(H_b \to \mu^- D^{*+} X) \times \mathcal{B}(D^{*+} \to D^0 \pi^+) \times \mathcal{B}(D^0 \to K^- \pi^+)$ for the $\mu^- D^{*+}$ mode. The generic b hadron, H_b, is an admixture of all weakly decaying b hadrons, including B^+, B^0, B_s^0, B_c^+, and Λ_b. To extract the H_b cross section, we utilize the measurement of the inclusive $H_b \to \mu^- D^0 X$ branching ratio from the DELPHI and OPAL experiments [14]. To apply this branching ratio to Tevatron data, we assume that the fragmentation fractions at high energy ($p_T(H_b) > 9\,\mathrm{GeV}/c$) are the same at LEP and the Tevatron. Charm branching ratios are taken from CLEO, ARGUS, and ALEPH measurements [15, 16].

Under the assumption that b and $\bar{b}$ quarks are produced in equal rates at the Tevatron, we include both $\mu^+ \overline{D}^0$ and $\mu^- D^0$ final states and introduce the factor of two in the denominator of Eq. (1) to report the cross section for a single b-hadron flavor.

To extract the number of candidate signal events, N, we reconstruct $H_b \to \mu^- D^0 X$ with $D^0 \to K^- \pi^+$, as well as $H_b \to \mu^- D^{*+} X$ with $D^{*+} \to D^0 \pi^+$ and $D^0 \to K^- \pi^+$, events using data that were acquired via a dedicated semi-muonic H_b trigger that requires a well measured muon and a track displaced from the primary vertex. The D^{*+} sample is a subset of the $D^0 \to K^- \pi^+$ sample. We use these two samples to make separate, but correlated, measurements.

The selection criteria are chosen to preferentially select H_b decays and reject combinatoric backgrounds. There are two types of physics backgrounds that exhibit a $\mu^- D$ signature that is similar to that of the expected signal. One arises from direct $p\bar{p} \to c\bar{c}X$ production where one charm quark decays to a muon and the other fragments into a D meson. The second physics background arises from $p\bar{p} \to b\bar{b}X$ events where one b hadron decays to a muon while the other decays to a D meson. The contributions from these sources are assessed using a combination of data and Monte Carlo (MC) simulation.

The acceptance α is determined by using MC simulation. We generate b quarks based on input distributions in transverse momentum, p_T, and rapidity, y, taken from theoretical calculations as well as previous cross section measurements. Fragmentation and decay are performed as part of the MC simulation. The passage of generated decay products in the CDF II detector is then simulated. Based upon the output of these simulated events, the fraction of produced events that fall within the active detector volume is calculated.

We factorize the determination of the trigger and detector efficiency, ϵ, into a product of relative efficiencies and an absolute efficiency. The advantage of this technique is that we can measure relative efficiencies from the data (as will be described in Section VI) and minimize our reliance on simulation.

The sensitivity of this analysis is limited by the systematic uncertainties. To limit our dependence on theoretical input and on detector simulation we estimate systematic uncertainties from data wherever possible.

III.   THE CDF II DETECTOR

The CDF II detector comprises a charged particle tracker in the magnetic field of a solenoid surrounded by a full coverage calorimeter and by muon detectors. In this section we give a short description of those detector components which are relevant to this analysis. A more detailed description of them and of the entire detector is given in Refs. [17–21].

We utilize a cylindrical coordinate system with the z axis oriented in the direction of the proton beam and the r-ϕ plane perpendicular to the beamline. We also define a polar angle, θ, measured from the z axis and pseudorapidity is defined as $\eta = -\ln[\tan(\theta/2)]$.

Two devices inside the 1.4 T solenoidal magnetic field are used for measuring the momentum of charged particles: the silicon vertex detector (SVX II) and the central tracking chamber (COT). The SVX II consists of double-sided microstrip sensors arranged in five cylindrical shells with radii between 2.5 and 10.6 cm. The SVX II detector is divided into three contiguous sections along the beam direction for a total z coverage of 90 cm. The COT is a cylindrical drift chamber containing 96 sense wire layers grouped into eight alternating superlayers of axial and stereo wires. The active volume covers $|z| < 155$ cm and 43 to 132 cm in radius.

The central muon detector (CMU) surrounds the central electromagnetic and hadronic calorimeters. The calorimeters have a depth corresponding to 5.5 interaction lengths. The CMU detector covers a pseudorapidity range $|\eta| < 0.6$ and is segmented into two barrels of 24 modules, each module covering $12.6°$ in ϕ. Every module is further segmented into three submodules, each covering $4.2°$ in ϕ and consisting of four layers of drift chambers. The smallest drift unit, called a stack, covers $1.2°$ in ϕ. Adjacent pairs of stacks are combined together into a tower. A track segment is identified by at least two hits out of the four layers of a stack. A second set of muon drift chambers, the CMP, covers the same η-range as the CMU and is located behind an additional steel absorber of ~ 3.3 interaction lengths. Muons which produce a track segment in both the CMU and CMP systems are called CMUP muons. A third set of muon drift chambers, the CMX, covers a pseudorapidity range $0.6 < |\eta| < 1.0$ and is separated by 6.2 interaction lengths from the nominal interaction point.

Luminosity is measured using gas Cherenkov counters (CLC) mounted at small angles to the beamline. The CLC measures the rate of inelastic $p\overline{p}$ collisions. The inelastic $p\overline{p}$ cross section at $\sqrt{s} = 1960$ GeV is scaled from measurements at $\sqrt{s} = 1800$ GeV using the calculations in Ref. [22]. The integrated luminosity is determined with negligible statistical uncertainty and a 6% systematic accuracy [23].

The CDF experiment uses a three-level trigger system. At level 1 (L1), data from every beam crossing are stored in a pipeline capable of buffering data from 14 beam crossings. The level 1 trigger either rejects events or copies them onto one of the four level 2 (L2) buffers. Events that pass the level 1 and level 2 selection criteria are sent to the level 3 (L3) trigger, a cluster of computers running a speed-optimized version of the offline event reconstruction code.

To select heavy flavor events, we rely heavily upon charged-particle tracking in the trigger. At level 1, charged tracks with $p_T \geq 1.5$ GeV/c and $|\eta| < 1$ are found by the extremely fast tracker (XFT) [24], which uses information from the axial wires in the COT to perform r-ϕ track finding with high efficiency ($> 90\%$) and good transverse momentum resolution ($\delta p_T/p_T^2 = 0.017$). The track extrapolation system (XTRP) takes the track information from the XFT and provides extrapolation information so that the XFT tracks can be matched to track segments found in the muon detectors [25]. Tracks are matched to track segments in the CMU, CMP and CMX to identify muon candidates at level 1.

At level 2, the Silicon Vertex Trigger (SVT) combines information from the axial layers of the SVX II with the charged-particle tracking information from the XFT. Owing to the high precision information from the silicon detector, the SVT provides a precise measurement of the track impact parameter d_0 (distance of closest approach to the beamline) in the transverse plane with a resolution of approximately 50 μm. This resolution arises from approximately equal contributions of 35 μm from resolution and intrinsic spread of the position of the $p\overline{p}$ interaction. Tracks with large impact parameter are utilized to identify heavy flavor decay and strongly reject light (u, d, s) quark events.

For the data sample utilized in this analysis, level 3 event reconstruction included full COT tracking but did not include tracking in the silicon detectors. Events accepted by the level 3 trigger are stored for subsequent analysis.

The flexibility of the CDF II trigger permits the selection of samples with no leptons (all hadronic modes), one lepton (semileptonic modes) and two leptons ($J/\psi \to \mu^+\mu^-$ and $\Upsilon \to \mu^+\mu^-$ events.) For this analysis we utilize all three types of triggers, and we describe them in the following section.

IV. TRIGGER PATHS

A single trigger path is defined as a specific set of level 1, level 2, and level 3 selection criteria in the CDF II trigger system. The primary trigger path utilized in this analysis is referred to as the μSVT path. Data acquired through other trigger paths are utilized in this analysis to determine the selection efficiencies described in Section VI.

μ**SVT Path.** At level 1, this path identifies a muon candidate with $p_T > 4$ GeV/c by requiring that an XFT track be matched to segments in the CMU and CMP detectors. At level 2 the trigger utilizes information from the SVT to identify displaced tracks. We require a single track (which is not the muon candidate) with $p_T > 2$ GeV/c and an impact parameter between 120 μm and 1 mm to be identified, where the impact parameter measured by the SVT is relative to the beamline as determined over a large sampling of events. At level 3, full event reconstruction is done, except for track reconstruction in SVX II. In order for the event to be accepted, level 3 requires confirmation of the muon identified at level 1 and confirmation of the XFT track identified at level 2. The invariant mass of the two tracks must be less than 5 GeV/c^2, the azimuthal opening angle between the two tracks, $\Delta\phi$, must be $2° < \Delta\phi < 90°$, and the tracks must be consistent with coming from the same $p\overline{p}$ interaction vertex.

Inclusive Muon Path. This trigger requires that one muon candidate with $p_T > 8\,\mathrm{GeV}/c$ be identified by the XFT, CMU, and CMP. This path provides a sample of $J/\psi \to \mu^+\mu^-$ decays where only one of the muons is required in the trigger. The second muon in the event is unbiased, and can be utilized to directly measure the efficiency of the trigger selection.

Heavy Flavor Path. This trigger path is for hadronic decays of H_b and D hadrons. Two oppositely charged XFT tracks with $p_T > 2\,\mathrm{GeV}/c$ and $\Delta\phi < 135°$ are required at level 1. Those tracks are then required to have $120\,\mu\mathrm{m} < d_0 < 1\,\mathrm{mm}$ as measured by the SVT at level 2. The level 3 selection requires confirmation of the level 2 quantities using full reconstruction. From this path, we select large samples of $D^+ \to K^-\pi^+\pi^+$, $D^+ \to \phi\pi^+ \to K^+K^-\pi^+$, and $D_s^+ \to \phi\pi^+ \to K^+K^-\pi^+$ decays. Since only two of the three tracks are required in the trigger, the third track is unbiased with respect to the trigger. We can therefore use this sample to measure the efficiency of the SVT.

H_b Semileptonic Backup Path. This trigger path is used to determine the level 3 selection efficiency. Its requirements are the same as the μSVT trigger, except that it has no requirements at level 3, and only a fraction of events that pass the level 1 and level 2 trigger requirements are recorded.

J/ψ Dimuon Path. The J/ψ trigger paths which require one muon in the CMU system and a second muon in either the CMU or CMX system are used to measure the SVX II offline efficiency. The J/ψ CMU-CMU trigger requires, at level 1, at least two CMU muons be found with $p_T > 1.5\,\mathrm{GeV}/c$. There are no additional selection criteria applied at level 2. At level 3, an opposite sign muon pair is required with invariant mass between $2.7\,\mathrm{GeV}/c^2$ and $4.0\,\mathrm{GeV}/c^2$, which is efficient for J/ψ and $\psi(2s)$ decays into dimuons. The two muon tracks must also have $|\Delta z_0| < 5\,\mathrm{cm}$ and $\Delta\phi_0 < 130°$, where Δz_0 is the separation of the two tracks along the beamline ($r = 0$) and $\Delta\phi_0$ is the separation of the two tracks in azimuth at $r = 0$. The J/ψ CMU-CMX trigger is similar, except that instead of two CMU muons, one CMU and one CMX muon must be identified. The CMX muon must have $p_T > 2.0\,\mathrm{GeV}/c$.

V. EVENT SELECTION

This analysis uses data derived from $83\,\mathrm{pb}^{-1}$ of $p\overline{p}$ collisions at $\sqrt{s} = 1.96\,\mathrm{TeV}$ that were collected between October 2002 and May 2003. Thanks to the trigger utilized in this analysis, this relatively small sample of data is sufficient to significantly improve upon previous cross section measurements in semileptonic channels, and yields a result that is limited by the systematic uncertainties.

We begin the signal reconstruction by requiring the candidate muon, pion, and kaon tracks to satisfy COT fiducial and quality selection criteria, which include requirements on the number of hits assigned to the track and a loose selection on fit quality of the track. Muon selection criteria are motivated by the trigger requirements. The muon track must have $p_T > 4\,\mathrm{GeV}/c$ and $|\eta| < 0.6$ and must be matched to CMU and CMP track segments that satisfy fiducial and quality selection criteria, which include requirements on the number of hits used in the track segment and the quality of the match between the central track and the CMP track segment [26]. The candidate muon must also be matched to a CMUP muon found by the level 1 trigger.

In order to reduce combinatoric background, the pion and the kaon candidates must have $p_T > 1.0\,\mathrm{GeV}/c$ and $|\eta| < 1.0$, must satisfy SVX II fiducial and quality cuts, which include requirements on the number of hits assigned to the track and a loose selection on the fit quality of the track [26]. The two tracks must both come from a common displaced vertex and be consistent with the decay of a charmed meson. In addition, at least one of the candidate tracks must be matched to an SVT track that passes the displaced-track-trigger requirements, have $120\,\mu\mathrm{m} < d_0 < 850\,\mu\mathrm{m}$, and have hits in all of the SVX II layers used by the SVT. The pion and kaon candidates as well as the pion and muon candidates must have opposite charges. We combine the pion and kaon candidates to form $D^0 \to K^-\pi^+$ candidates. We form the combined momentum vector of the muon and the D^0 candidate and require that this vector have $|\eta(\mu^-D^0)| < 0.6$. The number of D^0 signal events is determined by fitting the $K^-\pi^+$ invariant mass distribution between $1.74\,\mathrm{GeV}/c^2$ and $1.98\,\mathrm{GeV}/c^2$ to a Gaussian peak plus a linear background.

The D^0 mass plots are shown for different regions of $p_T(\mu^-D^0)$ in Fig. 1. While the signal yield is rather low in the highest p_T region, clean signals are observed in the lower p_T regions. The signal yields are reported in Table I. Figure 2 shows the D^0 mass distribution for all events with $p_T(\mu^-D^0) > 9.0\,\mathrm{GeV}/c$ and $|\eta(\mu^-D^0)| < 0.6$.

For the decay $D^{*+} \to D^0\pi^+$, $D^0 \to K^-\pi^+$, the muon and D^0 reconstruction is the same as described above. We additionally require the presence of the pion from the $D^{*+} \to D^0\pi^+$ decay with $p_T > 400\,\mathrm{MeV}/c$ and $|\eta| < 1.0$ that passes COT fiducial and quality selection criteria. Since this pion tends to have low p_T, we refer to this as the "soft pion" (π_{soft}.) We require that the muon and soft pion have opposite charges and only consider events where the $K^-\pi^+$ invariant mass is between $1.82\,\mathrm{GeV}/c^2$ and $1.90\,\mathrm{GeV}/c^2$. As can be seen in Fig. 1, this mass window is wide enough so that no real D^0 decays are lost. We require $|\Delta z_0|$ between any two of the decay products of the H_b must be less than $5\,\mathrm{cm}$. In order to minimize the background, we look at the mass difference Δm between the $K^-\pi^+\pi^+_{soft}$ and the $K^-\pi^+$. We fit the mass difference distribution to a Gaussian plus the background shape $a\sqrt{\Delta m - m_\pi}\,e^{b(\Delta m - m_\pi)}$, where a and b are free parameters in the fit to the data. The mass difference plots are shown in Fig. 3. In order

to make comparisons between the two measurements, we present the data in p_T bins of the $\mu^- D^0$ system. The yields are included in Table I. Figure 4 shows the mass difference for all events with $p_T(\mu^- D^0) > 9.0$ GeV/c and $|\eta(\mu^- D^0)| < 0.6$.

VI. EFFICIENCY MEASUREMENTS

The efficiencies of the CDF II trigger and detector components for the cross section measurement are determined whenever possible by using data collected by complementary trigger paths. The trigger paths utilized are described in Section IV.

We have separated the overall efficiency, ϵ, into nine separate measurements, denoted ϵ_1-ϵ_9. The first eight terms are extracted using relative efficiencies and the ninth term is measured as an absolute efficiency. To calculate ϵ_8, we measure the efficiency for events to pass selection criterion eight *relative* to events which already have passed criterion nine. This yields $\epsilon_8 = \epsilon_8^{rel} \epsilon_9$. Repeating this procedure for selection criterion seven, we calculate the relative efficiency for events to pass selection seven relative to events that have already passed selections eight and nine: $\epsilon_7 = \epsilon_7^{rel} \epsilon_8$. Repeating this process for each of the selection criterion, we arrive at a final efficiency which is:

$$\epsilon = \epsilon_9 \prod_1^8 \epsilon_i^{rel}. \tag{2}$$

The absolute efficiency measurement (ϵ_9) is the efficiency for finding a charged-particle track in the central outer tracker (COT). This absolute efficiency is determined using a combination of data and MC simulation based upon GEANT [27]. A brief description of these efficiency measurements is provided below. Details of all of the efficiency measurements and parameterizations may be found in Ref. [26]. We perform these measurements in bins of kinematic variables. For example, the level 1 trigger efficiency depends upon the momentum of the muon. The efficiency corrections are then applied according to the kinematics of each event.

A. Level 1 Efficiency (ϵ_1)

For the μSVT trigger path, the level 1 muon trigger requirement consists of an XFT track with $p_T > 4$ GeV/c that is matched to track segments in the CMU and CMP subdetectors. We measure the efficiency of this trigger with respect to the offline CMUP muon reconstruction efficiency. To do this, we reconstruct the $J/\psi \to \mu^+\mu^-$ signal in events that were collected via the inclusive muon trigger path. The trigger muon ($p_T > 8$ GeV/c) in these events is biased for the efficiency measurement, but the other decay muon of the J/ψ can be used to determine the trigger efficiency. We refer to the J/ψ decay muon that is unbiased by the trigger as the "probe" muon, since it can be used to directly measure the trigger efficiency. We then compare the number of times the probe muon satisfied the trigger to the number of probe muons which were within the acceptance of the trigger.

We require both muons of the J/ψ to pass COT, CMU, and CMP fiducial and quality selection criteria. The probe muon must also have $|\eta| < 0.6$ and $p_T > 4$ GeV/c. We find a signal yield of approximately 1900 events. Sideband subtraction is used to parameterize the efficiency in terms of muon p_T and η. We find the plateau efficiency ($p_T \gtrsim 5$ GeV/c) to be 90%.

B. Level 2 XFT Efficiency (ϵ_2)

For the μSVT signal path, the XFT tracks found in level 1 are used as input for the level 2 SVT trigger. The trigger path requires at least one XFT track, not associated with the muon candidate, having $p_T > 2$ GeV/c; the SVT further requires that the impact parameter for this track be between 120μ m and 1 mm. The overall efficiency of this selection is given by the product of the XFT and SVT efficiency. We require that either the kaon or pion from the D^0 decay satisfy this selection.

The XFT efficiency is measured for pions and kaons with $p_T > 2.0$ GeV/c and $|\eta| < 1.0$. Given their different ionization energy losses, we treat kaons and pions separately in this measurement. In order to obtain pure samples of kaons and pions, we reconstruct $D^+ \to K^-\pi^+\pi^+$ events, $D^+ \to \phi\pi^+$, $\phi \to K^+K^-$ events, and $D_s^+ \to \phi\pi^+$, $\phi \to K^+K^-$ events that were collected by the heavy flavor trigger path. We have roughly 200 000, 9500, and 18 000 signal events respectively in the three modes. Two of the tracks from each decay are required to pass the trigger

requirements, and the third track is used to probe the XFT efficiency. We apply both COT and SVX II fiducial and quality selection criteria on the tracks that fired the trigger, and COT fiducial and quality selection criteria on the tracks used to probe the XFT efficiency. For the resonant decays, a cut is placed at $\pm 10\,\mathrm{MeV}$ around the ϕ mass. Sideband subtraction is used to measure the pion and kaon yields. We parameterize the efficiencies in terms of p_T, η and ϕ. We additionally parameterize the XFT efficiencies over the time which the data was acquired. The average efficiencies are approximately 90% for pions and 85% for kaons.

C. Level 2 SVT Efficiency (ϵ_3)

The second component of the level 2 trigger efficiency is the SVT efficiency for tracks that have already been identified by the XFT. The SVT efficiency does not depend on the particle species, so we measure the efficiency using a high statistics sample of $J/\psi \to \mu^+\mu^-$ events that were collected by the inclusive $p_T > 8\,\mathrm{GeV}/c$ muon trigger path. The technique here is similar to the technique utilized to measure the level 1 efficiency.

We use tracks that have $p_T > 2.0\,\mathrm{GeV}/c$, $|\eta| < 1.0$, and $120\ \mu\mathrm{m} < |d_0| < 850\ \mu\mathrm{m}$. The muon from the J/ψ which did not satisfy the trigger is used as the probe track. On events where both muons satisfy the $p_T > 8\,\mathrm{GeV}/c$ inclusive muon trigger, both muons are used as probe tracks. We impose COT and SVX II fiducial and quality selection criteria on the probe track, and require the track to be matched to an XFT track. Therefore the SVT efficiency is measured relative to a track found offline with the required number of SVX II hits. There are approximately 71 000 tracks that pass these selection criteria. The efficiency is parameterized in terms of p_T, d_0, and track isolation, which is a measure of the number of tracks found within an angular region of $\delta\phi < 5°$. For tracks with $p_T \gtrsim 3\,\mathrm{GeV}/c$, the plateau efficiency for the SVT is approximately 90%. The η dependence of the efficiency is small, and further mitigated because the tracks used in the efficiency measurement sample the detector in a manner similar to the signal. Since the SVX II hit efficiency is not part of the level 2 SVT efficiency calculation (it contributes to the SVX II efficiency described below) the inefficiency here is dominated by the track-finding and fitting algorithms utilized in the SVT.

The track isolation dependence of the SVT efficiency requires special treatment. The occupancy in the silicon detector arises from a number of sources, including very low momentum tracks from the underlying $p\bar{p}$ interaction along with a spectrum of tracks originating from multiple $p\bar{p}$ interactions. These effects are not modeled reliably in the Monte Carlo simulation, and so we reweight the data based on the isolation of the signal events. In addition to the raw yields, Table I also lists the yields after correction for the SVT efficiency.

D. Level 3 Efficiency (ϵ_4)

At level 3, our trigger path requires that a muon with $p_T > 4\mathrm{GeV}/c$ be reconstructed. In addition, a track identified in the COT (other than the muon) must be matched to an SVT track meeting the level 2 trigger requirements. The muon track and COT-SVT track must have an invariant mass of less than $5.0\,\mathrm{GeV}/c^2$ and $2.0° < \Delta\phi_0 < 90°$. To find the efficiency of this trigger, we look at $\sim 30\ 000$ events that were acquired on the H_b semileptonic backup path. We parameterize the efficiency in terms of the p_T of the muon and the p_T of the SVT track. For muons with $p_T \gtrsim 4.5\,\mathrm{GeV}/c$, the level 3 efficiency is approximately 97%.

E. SVX II Efficiency for Triggered Pions and Kaons (ϵ_5)

In order to determine the efficiency for attaching SVX II hits to a COT track, we look at muon tracks from $J/\psi \to \mu^+\mu^-$ decays collected on the J/ψ dimuon trigger path. We use this sample in order to have a large sample of tracks with negligible fake rate. The tracks are required to pass COT quality and fiducial, as well as SVX II, selection criteria. We consider only tracks that are expected to pass through the four layers of the SVX II used in the SVT trigger. The average efficiency is observed to be 80%, where the inefficiency is dominated by dead silicon ladders and poor efficiency near the ends of the silicon ladders. To account for the dependence on SVX II coverage, we correct the efficiency as a function of the z position of the track at its origin.

F. SVX II Efficiency for Untriggered Pions and Kaons (ϵ_6)

We require hits in at least three layers of the SVX II on the D^0 decay track that is not required by the trigger. We find the efficiency by looking in our signal sample with and without the SVX II hit requirement for the second track.

This yields an SVX II efficiency for the untriggered track of $(93.2 \pm 1.0)\%$. The efficiency for the untriggered track is higher than that for the triggered track because of the looser requirement on the number of SVX II hits.

G. CMU efficiency (ϵ_7)

In order to find the efficiency for linking a muon COT track to a CMU track segment, we reconstruct $J/\psi \to \mu^+\mu^-$ events using both the inclusive muon and semileptonic backup trigger paths. The muon tracks must pass COT fiducial and quality selection criteria. One of the decay muons from the J/ψ must satisfy the muon trigger requirements. For events acquired on the semileptonic backup trigger path, the probe track must satisfy the SVT trigger requirements. The probe tracks are extrapolated to the CMU, and are required to pass CMU fiducial selection criteria. The probe tracks must have $p_T > 4.0 \, \text{GeV}/c$ and $|\eta| < 0.6$. The efficiency is found to be independent of p_T, ϕ, and η, and so we use a single efficiency value of $(79.5 \pm 1.3)\%$.

H. CMP efficiency (ϵ_8)

We find the efficiency for linking a CMP track segment to a COT track that has already been linked to a CMU track segment by reconstructing $J/\psi \to \mu^+\mu^-$ candidates in events collected by the J/ψ dimuon trigger path. This trigger path does not require hits in the CMP, so either decay muon from the J/ψ can be used to probe the CMP efficiency. We require the muon to pass COT and CMU fiducial and quality selection criteria. The muon is extrapolated out to the CMP and required to pass CMP fiducial selection criteria. We examine only muons with $p_T > 4.0$ GeV/c and $|\eta| < 0.6$. The efficiency is parameterized in terms of p_T and η. The average CMP efficiency is 85%.

I. COT efficiency (ϵ_9)

To determine the absolute COT track finding efficiency, we use a combination of data along with a detailed MC simulation of the CDF II tracking system.

First, we use a MC simulation only technique to compare charged particles generated by the PYTHIA MC program to charged tracks reconstructed after full MC detector simulation and event reconstruction. This yields our measurement of absolute COT track finding efficiency.

To assess the systematic uncertainty on this measurement, we use a combination of data and MC simulation to "embed" simulated MC kaons, pions and muons into data events acquired via the inclusive muon trigger path. The MC simulated COT hits from the simulated track are incorporated into the detector data from a real event. To accurately emulate track reconstruction in $\mu^- D^0$ events, the embedded MC simulated track is placed within a region in η-ϕ space that is within $\sqrt{\delta\eta^2 + \delta\phi^2} < 1.4$ of the trigger muon. The hybrid event, which consists of data plus hits from a single simulated track, is then reconstructed in the same way as our signal sample. The simulated track is considered to be correctly found if a reconstructed track is matched closely in p_T and ϕ to the simulated track embedded in the event.

We vary the matching criteria to assess the rate at which tracks may be found but reconstructed with incorrect parameters. For tracks with $p_T > 1.0 \, \text{GeV}/c$ (which includes all muons and kaons, and the pions from the decay of the D^0), the track-finding efficiencies derived from MC-only simulation and track embedding agree to within 1% and are insensitive to the details of the matching criteria. The COT efficiency for muons is approximately 99%. For pions and kaons with $p_T > 2 \, \text{GeV}/c$ the COT efficiency is greater than 90%. For pions with $p_T < 1.0 \, \text{GeV}/c$, which are used in reconstructing the $D^{*+} \to D^0\pi^+$ decay, we observe a significant difference in efficiency estimates from the different techniques, and we use these variations to assess a systematic uncertainty on the low p_T efficiency measurement. It is additionally necessary to account for uncertainty in the amount of material in the inner detector region, which also affects the absolute track finding efficiency. We make a conservative estimate of the systematic uncertainty by varying the total amount of material by 25%. This rather large variation in the amount of passive material in the detector translates into a systematic uncertainty on the tracking efficiency of approximately 2.6%.

J. Efficiency Summary

For a given signal event which is within the acceptance of the detector, the absolute efficiency to reconstruct the event is the product of the efficiency terms outlined in this section. In many cases, the efficiency depends upon the track momentum as well as its position within the detector. The details of these efficiency parameterizations can be

found in Ref. [26]. For signal events which are well away from turn-on effects, the overall trigger and reconstruction efficiency is approximately 35%.

VII. ACCEPTANCE

Our detector acceptance is defined by the selection criteria and the active regions of the detector which cover those criteria. We determine the detector acceptance from MC simulation by first generating single b hadrons according to measured momentum and rapidity spectra. These hadrons are then decayed using the EVTGEN package [28] and then fed into a GEANT simulation of the detector. The MC simulation of the detector is utilized to map out the active regions of the detector. At this stage, we are not using the simulation to quantify detector inefficiencies, since those are measured using techniques described in the previous section. We generate b hadrons based upon two distinct distributions in transverse momentum and rapidity. The first is based on NLO [1, 2] QCD theory with MRSD$_0$ parton distribution function [29], a b quark mass of $4.75\,\mathrm{GeV}/c^2$, and renormalization and factorization scales equal to $\sqrt{m_b^2 + p_T^2}$. Peterson fragmentation is used, with $\epsilon_P = 0.006$. The other spectrum is based on the measured $H_b \rightarrow J/\psi X$ cross section [8], which we refer to below as the "CDF MC sample." We use the production fractions $f_u : f_d : f_s$ of 1:1:0.270 [30]. We assume that Λ_b decays provide a negligible contribution to our signal because of the low probability for a semleptonic b-baryon decay that would also yield a D^0 meson.

To demonstrate the degree to which the MC simulation reproduces the data, Figs. 5(a,b,c) show the p_T distributions of the $\mu^- D^0$, μ, and D^0 for the MC simulation after all selection criteria and efficiencies have been applied, and for data after all selection criteria and corrections for the SVT efficiency. The data are seen to have higher $p_T(\mu^- D^0)$ than the MC simulation based upon the $H_b \rightarrow J/\psi X$ cross section result [8], while they are seen to have lower $p_T(\mu^- D^0)$ than the spectrum from the MRSD$_0$ MC simulation, referred to below as the "MRSD$_0$ MC sample." We therefore measure the cross sections by taking the average of the cross sections from the two methods and assign one-half the difference as a systematic uncertainty.

We perform additional comparisons between the data and the two MC simulated samples. Distributions such as $\eta(\mu^- D^0)$, $p_T(\mu^-)$, and $p_T(D^0)$ are all seen to agree well between the data and both MC simulated samples. These comparisons can be found in Ref. [26]. Table II shows the acceptance times efficiency (excluding the SVT efficiency) as a function of $p_T(H_b)$ bin calculated using the CDF and MRSD$_0$ samples [26].

There is significant uncertainty in the branching ratios for $H_b \rightarrow \mu^- \rightarrow D^{**}X$ where the D^{**} decays to $D^0 X$. An incorrect modelling of this fraction can affect the $p_T(\mu^- D^0)$ spectrum and therefore the acceptance. To conservatively assess the systematic uncertainty on the measured cross section, we modify $\mathcal{B}(H_b \rightarrow \mu^- D^{**})$ by $\pm 50\%$.

VIII. BACKGROUNDS

While fitting the D^0 peak to a Gaussian allows us to determine how many $\mu^- D^0$ events are in our sample and account for non-charm background, it is possible that there are real $\mu^- D^0$ events that are not part of our $H_b \rightarrow \mu^- D^0$ signal. One source of this background is direct $c\bar{c}$ production. It is possible for direct charm to mimic our signal by having one charm quark decay to a muon, and the other charm quark fragment into a D^0. The second background source is $b\bar{b}$ production, where one b hadron decays to $D^0 X$, and the other b hadron follows the decay chain $H_b \rightarrow D \rightarrow \mu^- X$. Since these background sources are irreducible, we estimate their contributions and correct the total number of observed signal events [26].

A. $c\bar{c}$ Background Estimate

In order to estimate the fraction of events in our sample from direct charm, we use the impact parameter of the D^0 [31]. As the D^0 mesons from direct charm are created at the primary vertex, they should point back to the primary vertex within an error determined by the detector resolution. The D^0 from b decays, on the other hand, are created at the secondary b vertex, and are less likely to point back at the primary vertex. The D^0 impact parameter distribution for our signal sample is shown in Fig. 6. Although dominated by D^0 from b-hadron decays, this distribution contains a prompt component arising from direct $c\bar{c}$ production. We use MC simulation to determine the expected impact parameter distributions for D^0 mesons from b-hadron production and direct production.

To determine the impact parameter distribution for D^0 mesons from b decays, we use the same MC simulated sample that is used to find the acceptance above. In order to get the d_0 distribution of the D^0 from direct charm, we generate $D^0 \rightarrow K^- \pi^+$ events originating from the primary vertex. The generated prompt $D^0 \rightarrow K^- \pi^+$ sample

has lower $p_T(D^0)$ than does our signal sample, so we reweight the p_T spectrum of the MC simulated D^0 so that it matches the $p_T(D^0)$ spectrum in $H_b \to \mu^- D^0$ events from the PYTHIA MC simulation [32].

In the direct charm and $H_b \to D^0$ samples, we calculate the impact parameter using generator level MC simulated quantities. In order to estimate the uncertainty on the D^0 impact parameter due to detector resolution, we look at the sideband subtracted D^0 impact parameter uncertainty distribution in our signal sample acquired on the μSVT trigger. We see that the average uncertainty is approximately 34 μm, so we smear the MC simulated impact parameters using a Gaussian resolution function with a standard deviation of 34 μm. We do a bin-by-bin χ^2 fit to determine the ratio of events from direct charm to those from b hardon decays. We find that using the d_0 distribution from the H_b events generated with the p_T spectrum measured in the CDF $H_b \to J/\psi X$ cross section measurement [8], we measure a charm fraction of $(6.3 \pm 2.1)\%$, while using the d_0 distribution from the b events in the MRSD$_0$ sample gives a charm fraction of $(5.4 \pm 2.1)\%$. So as a final result, we use the average charm fraction of $(5.9 \pm 2.1(\text{stat}) \pm 0.4(\text{syst}))\%$.

For the differential cross section, we must also account for the p_T spectrum of $\mu^- D^0$ candidates arising from direct $c\bar{c}$ production. For normalization, we use the total $c\bar{c}$ yield as calculated above. To determine the $p_T(D^0)$ spectrum, we use MC simulation, where the generated events are reweighted to match the predicted direct charm spectrum [33]. From this reweighted MC sample, we estimate the bin-by-bin contribution from direct $c\bar{c}$ background.

B. $b\bar{b}$ Background Estimate

The presence of $b\bar{b}$ events can mimic the signal in the cases where the μ^- and D^0 come from different b hadrons. An example of this is where the b hadron decays as $b \to D^0 X$ and the other follows the decay chain $\bar{b} \to \bar{c} \to \mu^- X$. This configuration provides a $\mu^- D^0$ candidate with the proper charge correlation, constituting an irreducible background to genuine $H_b \to \mu^- D^0$ decays.

To investigate this background source, we look at events where one b hadron decays to a D^0 meson, and the other follows the decay chain $\bar{b} \to \mu^+ X$, providing the wrong-sign $\mu^+ D^0$ combination. The right-sign $b\bar{b}$ background is then estimated by counting wrong-sign $\mu^+ D^0$ events and correcting this by the expected ratio of the two decay chains $\bar{b} \to \mu^+$ and $\bar{b} \to \bar{c} \to \mu^-$.

We begin by looking for wrong-sign $\mu^+ D^0$ events, where we have a $D^0 \to K^- \pi^+$ peak in events where the pion and muon have the same charge, $q_\mu = q_\pi$. This is complicated by two factors. First, there is a large background in the wrong-sign sample from real $\mu^- D^0$ signal events where the $D^0 \to K^- \pi^+$ decay is incorrectly reconstructed as $\overline{D^0} \to K^+ \pi^-$. The reflection does not yield a narrow D^0 peak in the pion-kaon invariant mass distribution but instead yields a broad peak which we parameterize using MC simulated D^0 decays. We use this parameterization and fix normalization of the reflection peak relative to the signal peak based upon the MC simulation. The MC simulated wrong-sign mass distribution is found to be insensitive to the input $p_T(b)$ spectrum.

The second complication is that the doubly Cabibbo-suppressed decay of the $D^0 \to K^+ \pi^-$ is also expected to yield a small peak in the K-π invariant mass distribution. Based upon measured branching ratios [30], the number of doubly Cabibbo-suppressed events is expected to be 0.0036 ± 0.0003 times the number of events in our signal peak. After correcting for these effects, we find a wrong-sign peak that is $(4.4 \pm 1.7)\%$ the size of the right sign peak.

To convert this number into an estimate of the number of right sign $b\bar{b}$ events, we look at a generator level sample of $b\bar{b}$ MC simulation generated using PYTHIA and decayed with EVTGEN using our best knowledge of branching ratios. In this sample, we look for events where one b decayed to a muon, and the other one produced a D^0. In order to get a sufficiently large event sample, we use somewhat looser selection criteria on the $b\bar{b}$ than are in our sample, and do not apply any of our efficiency measurements to the events. We find the ratio to be $N(\bar{b} \to \bar{c} \to \mu^-)/N(\bar{b} \to \mu^-) = 0.23 \pm 0.02\,(\text{stat})$. To take into account the effect of the looser event selection criteria, we apply a 50% systematic, giving a final ratio of $0.23 \pm 0.02(\text{stat}) \pm 0.11(\text{syst})$. Combining this result with the wrong-sign contribution of $(4.4 \pm 1.7)\%$ yields a $b\bar{b}$ background fraction of $(1.0 \pm 0.40 \pm 0.48)\%$.

C. $H_b \to DD$ and $H_b \to D\tau$ Backgrounds

In addition to backgrounds from $c\bar{c}$ and $b\bar{b}$ events, a background also comes from the decays of a single b hadron. These events can occur when the decay $b \to c\bar{c}s$ or $b \to c\bar{c}d$ is followed by one of the charm quarks decaying to a muon, and the other decaying through $D^0 \to K^- \pi^+$. These events also can come from a decay of $b \to c\tau^- \bar{\nu}_\tau$, where the tau lepton decays to a muon, and the c decays through $D^0 \to K^- \pi^+$. Because these events come from real H_b decays, the impact parameter of the D^0 will not necessarily be consistent with production at the primary vertex. The muon and the pion from the decay will have opposite charges, as is the case in $b \to c\mu^- \bar{\nu}_\mu$ events. We account for this contribution by retaining events with $H_b \to DD$ and $H_b \to D\tau$ decays in the MC simulation utilized for the acceptance measurement and correct for it in the unfolding procedure described in Sect. IX. Since the branching

fractions for some of these decays are not well known, we allow the number of events from $H_b \to DD$ and $H_b \to D\tau$ to vary by $\pm 50\%$, which translates in a 2.5% systematic uncertainty on the measured cross section.

D. Fake Muons

In fitting the D^0 mass distribution, we account for combinatoric background using the sidebands of the mass distribution. This technique is not available for hadrons that are misidentified as muons, so we must estimate the contribution of fake muons independently.

For $c\bar{c}$ background events described above, the background is assessed by looking at the impact parameter of the D^0, independent of whether the muon is real or fake. Therefore, the only source of fake muons that we must account for are fake muons reconstructed in association with real $H_b \to D^0 X$ decays. To evaluate this, we use a sample of $D^+ \to K^- \pi^+ \pi^+$ decays from the heavy flavor trigger path that is enhanced in $H_b \to D^+ X$ decays. We measure the rate of tracks near the D^+ which are fiducial to the CMU and CMP detectors and have $p_T > 3 \,\mathrm{GeV}/c$. Due to their smaller nuclear interaction cross section, kaons are misidentified as muons at a higher rate than pions. To conservatively assess a muon misidentification rate, we assume that all of these tracks are kaons. We then apply a 0.5% probability that a fiducial kaon is reconstructed as a muon, as measured in Ref. [34]. From this, we determine that the rate of fake muons in our signal sample is approximately 0.05%, small enough to neglect.

IX. $H_b \to \mu^- D^0 X$ CROSS SECTION

In order to extract the b-hadron differential cross section from the measured $p_T(\mu^- D^0)$ distribution, we unfold the observed $p_T(H_b)$ distribution on the basis of the MC simulated signal. We determine a weight, w_{ij}, that is defined as

$$w_{ij} = \frac{N([H_b]_i \to [\mu^- D^0]_j)}{N([\mu^- D^0]_j)}, \tag{3}$$

where $N([H_b]_i \to [\mu^- D^0]_j)$ is the number of b hadrons with $|y| < 0.6$ in $p_T(H_b)$ bin i decaying to $\mu^- D^0$ in $p_T(\mu^- D^0)$ bin j which pass all selection criteria and $N([\mu^- D^0]_j)$ is the number of $\mu^- D^0$ events in $p_T(\mu^- D^0)$ bin j which pass all selection criteria.

We generate MC simulated H_b events with $|y(H_b)| < 0.8$ as described in Section VII to properly model the detector acceptance. We also include events where the $\mu^- D^0$ is produced via a $H_b \to DD$ or $H_b \to D\tau$ decay in the denominator in order to take that background into account. For the determination of the weights w_{ij}, it is the shape of the $p_T(H_b)$ distribution, not its absolute normalization, that matters. We list the weights from the CDF and MRSD_0 MC simulated samples in Tables III and IV. Then, to unfold the number of b hadrons $N_i^{H_b}$ in a given $p_T(H_b)$ bin i we use the formula:

$$N_i^{H_b} = \sum_{j=1}^{N} w_{ij} N_j^{\mu^- D^0}, \tag{4}$$

where $N_j^{\mu^- D^0}$ is the number of events in $p_T(\mu^- D^0)$ bin j from data, shown in Table I. We now have all of the terms from Eq. (1) required to extract the cross section.

The statistical uncertainty on the cross section for $p_T(H_b)$ bin i is given by

$$\delta_{stat}^2(\sigma_i) = (\delta N_i^{H_b})^2 \left[\sum_{j=1}^{N} \frac{w_{ij}}{\alpha_i \epsilon_i \mathcal{L}} \right]^2, \tag{5}$$

where α_i and ϵ_i are the acceptance and efficiency for the bin i respectively. The statistical uncertainty on the total cross section is obtained by summing the uncertainties in quadrature over all bins of $p_T(H_b)$.

We check the analytical calculation of the statistical uncertainty using MC simulated pseudo experiments which model the signal and background distributions along with bin migration of the signal. We verify that the MC simulation yields the same statistical uncertainty on the differential and integrated cross section as we observe using the above analytical formula. The uncertainty is calculated by generating 1000 distinct MC simulated experiments

corresponding to the total sample $\mu^- D^0$ yield we observe. The distribution of fitted yields in each p_T bin is observed to be gaussian, and we take the standard deviation of the distribution to be the statistical uncertainty in each bin.

The systematic uncertainties are determined in general by varying the efficiency or acceptance in question by $\pm 1\sigma$ and calculating the shift in the measured cross section. In the case of the efficiency measurements, which are parameterized based upon fits to the data (*e.g.* , the level 1 trigger efficiency is parameterized as a function of muon p_T and η) the variation in efficiency is taken from the error matrix determined in the fits.

Using this technique, the uncertainty derived based upon the SVT efficiency fit appears to be underestimated. The variation in the measured points is not reflected by the statistical uncertainty in the fit for the SVT efficiency. In this case, we assess the systematic uncertainty by replacing the fitted efficiency with the bin-by-bin points that are derived in the efficiency measurement. The difference between the result and the value obtained from the SVT efficiency data points is taken as a fit modelling uncertainty and combined in quadrature with the 1σ systematic uncertainty described above to obtain the total systematic uncertainty [26].

The systematic uncertainty on the MC simulated p_T spectrum is estimated by taking the fractional difference between the cross section found using the $H_b \rightarrow J/\psi X$ and the reweighted MRSD$_0$ NLO MC simulated samples. The degree to which final state radiation affects the D^0 lineshape is assessed with the PHOTOS MC simulation [35]. Systematic uncertainty contributions are shown in Table V. It is worth noting that the systematic uncertainty arising from the MC simulated p_T shape on the total cross section is less than the systematic uncertainty due to the MC simulation p_T shape in most of the p_T bins. This is because uncertainty on the p_T shape primarily affects the fraction of the total cross section in a specific p_T bin. When integrating over all bins, this effect is diluted. Also, when finding the acceptance for a specific p_T bin, one can only use the MC simulated events within that bin, while the overall measurement uses all of the MC simulated events. This leads to a lower statistical uncertainty in the MC simulated samples.

After applying all corrections to the data, we obtain the total cross section times branching ratio

$$\sigma(p\overline{p} \rightarrow H_b X) \times \mathcal{B}(H_b \rightarrow \mu^- D^0 X) \times \mathcal{B}(D^0 \rightarrow K^- \pi^+) = 3.46 \pm 0.14(\text{stat})^{+0.36}_{-0.38}(\text{syst})\,\text{nb}$$

for b hadrons with $p_T > 9\,\text{GeV}/c$ and $|y| < 0.6$. Using the current world average branching ratios $\mathcal{B}(H_b \rightarrow \mu^- D^0) = (6.84 \pm 0.35)\%$ [14, 30] and $\mathcal{B}(D^0 \rightarrow K^- \pi^+) = (3.89 \pm 0.05)\%$ [15, 30], we measure a total cross section of

$$\sigma(p\overline{p} \rightarrow H_b X) = 1.30 \pm 0.05(\text{stat}) \pm 0.14(\text{syst}) \pm 0.07(\mathcal{B})\,\mu\text{b}$$

for b hadrons with $p_T > 9\,\text{GeV}/c$ and $|y| < 0.6$. The differential cross section times branching ratio is shown in Table VI, and displayed in Fig. 7(a). Figure 7(b) shows the differential cross section.

X. $H_b \rightarrow \mu^- D^{*+} X$ CROSS SECTION

For the $H_b \rightarrow \mu^- D^{*+}$, $D^{*+} \rightarrow D^0 \pi^+$, $D^0 \rightarrow K^- \pi^+$ channel, the efficiencies are the same as those for the $H_b \rightarrow \mu^- D^0$, $D^0 \rightarrow K^- \pi^+$, except that we must additionally account for the soft pion identification efficiency.

The systematics for the D^{*+} measurement are the same as those for the D^0 measurement listed in Table V unless mentioned specifically.

After applying all corrections to the data, we obtain the total cross section times branching ratio $H_b \rightarrow \mu^- D^{*+}$, with $D^{*+} \rightarrow D^0 \pi^+$ and $D^0 \rightarrow K^- \pi^+$ decays of

$$\sigma(p\overline{p} \rightarrow H_b X) \times \mathcal{B}(H_b \rightarrow \mu^- K^- \pi^+ \pi^+ X) = 1.05 \pm 0.08(\text{stat})^{+0.13}_{-0.15}(\text{syst})\,\text{nb},$$

for b hadrons with $p_T > 9\,\text{GeV}/c$ and $|y| < 0.6$ and using the notation $\mathcal{B}(H_b \rightarrow \mu^- K^- \pi^+ \pi^+ X)$ as shorthand for the product of $\mathcal{B}(H_b \rightarrow \mu^- D^{*+})$, $\mathcal{B}(D^{*+} \rightarrow D^0 \pi^+)$, and $\mathcal{B}(D^0 \rightarrow K^- \pi^+)$. Using the current world average branching ratios $\mathcal{B}(H_b \rightarrow \mu^- D^{*+}) = (2.75 \pm 0.19)\%$ [14, 30], $\mathcal{B}(D^{*+} \rightarrow D^0 \pi^+) = (67.7 \pm 0.5)\%$ [16, 30], and $\mathcal{B}(D^0 \rightarrow K^- \pi^+) = (3.89 \pm 0.05)\%$ [15, 30], we find a total cross section of

$$\sigma(p\overline{p} \rightarrow H_b X) = 1.45 \pm 0.11(\text{stat})^{+0.18}_{-0.21}(\text{syst}) \pm 0.10(\mathcal{B})\,\mu\text{b}$$

for b hadrons with $p_T > 9\,\text{GeV}/c$ and $|y| < 0.6$. The differential cross section times branching ratio is shown in Table VII, and displayed in Fig. 8. We also show the differential cross section using branching ratios measured

elsewhere.

We consider the $H_b \to \mu^- D^{*+} X$ cross section results to be a modest extension and cross check of the primary $H_b \to \mu^- D^0 X$ cross section result presented in this paper. The $\mu^- D^{*+} X$ sample is of limited statistical power and, being a subset of the $\mu^- D^0 X$ sample, there is nothing to be gained by averaging the two results.

XI. COMPARISON WITH THEORY AND PREVIOUS MEASUREMENTS

Our results agree well with previous measurements of the H_b cross section at CDF [8] and with the predictions of FONLL [10]. The CDF collaboration previously measured the H_b cross section using $H_b \to J/\psi X$ of $1.34 \pm 0.07\mu$b in the same range of p_T and y [8]. The FONLL prediction for the total cross section with $p_T(b) > 9.0\,\mathrm{GeV}/c$ and $|y| < 0.6$ is $1.39^{+0.49}_{-0.34}\mu$b [10]. Figure 9 shows the differential cross sections plotted together.

To compare these results with the cross section measured in the exclusive decay channel $B^+ \to J/\psi K^+$ [12], we must account for the different rapidity ranges. Reference [12] measured the cross section for $|y| < 1$, while the result presented here and the inclusive $J/\psi X$ result from Ref. [8] measure the cross section for $|y| < 0.6$. Figure 10 shows the comparison between these results, where we have scaled all cross sections to $|y| < 1$ assuming that inclusive H_b production is flat in rapidity. Furthermore, we correct for the differences in fragmentation fractions for B^+ (f_u) and H_b ($f_u + f_d + f_s$) [36]. Figure 10 shows good agreement between these recent b-hadron cross section measurements at $\sqrt{s} = 1.96\,\mathrm{TeV}$, as well as agreement between these complementary measurements and the FONLL prediction.

The trigger and analysis strategy shown here for the $\mu^- D^0$ and $\mu^- D^{*+}$ final state are quite different than those utilized in measurements using J/ψ final states. In addition to being statistically independent, many of the systematic uncertainties of this result are distinct from those of previous measurements. This result therefore provides a unique and independent measurement of the H_b cross section at the Tevatron.

XII. CONCLUSION

We have measured the b-hadron production cross section in $H_b \to \mu^- D^0 X$ and $H_b \to \mu^- D^{*+} X$ decays using the CDF II detector at the Fermilab Tevatron. The muon plus charm hadron decay signature was acquired using a dedicated trigger which takes advantage of the muon signature as well as the long H_b lifetime. By selecting an event sample based upon decay length information measured in the trigger, it is possible to acquire clean H_b signal samples at lower $p_T(H_b)$ than have been measured before. Complementary data samples are used to measure the trigger efficiencies for this analysis and Monte Carlo simulation is used to measure the acceptance. After accounting for backgrounds which mostly arise from heavy flavor ($b\overline{b}$ and $c\overline{c}$ production) the cross section is measured to be:

$$\sigma(p\overline{p} \to H_b X) = 1.30 \pm 0.05(\mathrm{stat}) \pm 0.14(\mathrm{syst}) \pm 0.07(\mathcal{B})\,\mu\mathrm{b}$$

for b hadrons with $p_T > 9\,\mathrm{GeV}/c$ and $|y| < 0.6$. We additionally present the differential cross section $d\sigma/dp_T$ which probes to lower $p_T(H_b)$ than have been measured before in semileptonic modes. We find the results presented here to be in good agreement with other recent measurements of the H_b cross section and in good agreement with fixed order next-to-leading logarithm calculations.

XIII. ACKNOWLEDGEMENTS

[1] P. Nason, S. Dawson, and R.K. Ellis. Nucl. Phys. **B303**, 607 (1988).

[2] P. Nason, S. Dawson, and R.K. Ellis. Nucl. Phys. **B327**, 49 (1989).

[3] M. Cacciari, M. Greco, and P. Nason. J. High Energy Phys., 9805 (1998) 007.

[4] D.Acosta *et al.* (CDF Collaboration), Phys.Rev. D **65**, 052005 (2002); F. Abe *et al.* (CDF Collaboration), Phys. Rev. Lett. **79**, 572 (1997); B. Abbott *et al.* (D0 Collaboration), Phys. Lett. B **487**, 264 (2000); B. Abbott *et al.* (D0 Collaboration), Phys. Rev. Lett. **85**, 5068 (2000).

[5] F. Abe *et al.* (CDF Collaboration), Phys. Rev. Lett. **71**, 500 (1993);

[6] F. Abe *et al.* (CDF Collaboration), Phys. Rev. Lett. **71**, 2396 (1993).

[7] S. Abachi *et al.* (D0 Collaboration), Phys. Rev. Lett. **74**, 3548 (1995).

[8] D. Acosta *et al.* (CDF Collaboration), Phys. Rev. D **71**, 032001 (2005).

[9] Rapidity is defined as $y = \frac{1}{2}\ln(\frac{E+p_z}{E-p_z})$.

[10] M. Cacciari *et al.*, J. High Energy Phys. **0407**, 033 (2004).

[11] M. L. Mangano, AIP Conf. Proc. **753**, 247 (2005); M. Cacciari, hep-ph/0407187.

[12] A. Abulencia *et al.* (CDF Collaboration), Phys. Rev. D **75**, 012010 (2007).

[13] F. Happacher *et al.*, Phys. Rev. D **73**, 014026 (2006).

[14] P.Abreu *et al.* (DELPHI Collaboration), Phys.Lett. B**475**, 407 (2000); R.Akers *et al.* (OPAL Collaboration), Z. Phys. C**67**, 57 (1995).

[15] B. Aubert *et al.* (B̸A̸B̸A̸R Collaboration), Phys. Rev. Lett. **100**, 051802 (2008); S. Dobbs *et al.* (CLEO Collaboration), Phys. Rev. D **71** , 112001 (2007); M. Artuso *et al.* (CLEO Collaboration), Phys. Rev. Lett. **80**, 3193 (1998); R. Barate *et al.* (ALEPH Collaboration), Phys. Lett. B **403**, 367 (1997); H. Albrecht *et al.* (ARGUS Collaboration), Phys. Lett. B **340**, 125 (1994); D. Decamp *et al.* (ALEPH Collaboration), Phys. Lett. B **266**, 218 (1991).

[16] J. Bartelt *et al.* (CLEO II Collaboration), Phys. Rev. Lett. **80**, 3919 (1998); H. Albrecht *et al.* (ARGUS Collaboration), Z. Phys. C **66**, 63 (1995); F. Butler *et al.* (CLEO Collaboration), Phys. Rev. Lett. **69**, 2041 (1992).

[17] D. Acosta *et al.* (CDF Collaboration), Phys. Rev. D **71**, 032001 (2005).

[18] A. Sill *et al.*, Nucl. Instrum. Methods Phys. Res., Sect. A **447**, 1 (2000).

[19] T. Affolder *et al.*, Nucl. Instrum. Methods Phys. Res., Sect. A **526**, 249 (2004).

[20] G. Ascoli *et al.*, Nucl. Instrum. Methods Phys. Res., Sect. A **268**, 33 (1988).

[21] D. Acosta *et al.*, Nucl. Instrum. Methods Phys. Res., Sect. A **494**, 57 (2002).

[22] M. M. Block and R. N. Cahn, Rev. Mod. Phys. **57**, 563 (1985).

[23] S. Klimenko *et al.*, Fermilab Report No. FERMILAB-FN-0741, 2003.

[24] E. J. Thomson *et al.*, IEEE Trans. on Nucl. Sci. **49**, 1063 (2003).

[25] R. Downing *et al.*, Nucl. Instrum. Methods A **570**, 36 (2007).

[26] J.A. Kraus, Ph.D. thesis, University of Illinois, 2006.

[27] R. Brun *et al.*, CERN Report No. CERN-DD-78-2-REV; R. Brun *et al.*, CERN Programming Library Long Write-up W5013 (1993).

[28] D. J. Lange, Nucl. Instum. Methods A **462**:152, 2001.

[29] A. D. Martin, W. J. Stirling, and R. G.Roberts, Phys.Rev. D**47**, 867 (1993).

[30] C. Amsler *et al.* (Particle Data Group), Phys. Lett. B **667** , 1(2008).

[31] D. Acosta *et al.* (CDF Collaboration), Phys. Rev. Lett.**91**, 241804 (2003).

[32] T. Sjostrand, S. Mrenna and P. Skands, J. High Energy Phys. **0605**, 26 (2006).

[33] M. Cacciari, private communication.

[34] T. Aaltonen *et al.* (CDF Collaboration), Phys. Rev. D**77**, 072004 (2008).

[35] E. Barberio and Z. Was, Comp.Phys.Comm. **79**, 291 (1994).

[36] A. Annovi, J.Phys.Conf.Ser. 110, 022003 (2008).

TABLE I: The signal yields for the number of D^0 and D^{*+} events per $p_T(\mu^- D^0)$ bin before (and after) correcting for SVT efficiency. Since the SVT efficiency depends upon the relative track isolation, a correction is performed based upon the topology of the signal events.

$p_T(\mu^- D^0)$ [GeV/c]	D^0 signal yield		D^* signal yield	
	measured	corrected	measured	corrected
9-11	867.9 ± 53.5	1040.6 ± 64.1	82.3 ± 10.5	96.1 ± 12.2
11-13	863.1 ± 45.8	1034.4 ± 54.9	142.6 ± 13.2	170.0 ± 15.7
13-17	1016.8 ± 46.3	1192.4 ± 54.3	236.4 ± 16.9	283.4 ± 20.2
17-29	669.6 ± 38.3	781.9 ± 44.7	169.6 ± 14.1	199.8 ± 16.6
29-40	67.0 ± 12.2	80.1 ± 14.6	14.3 ± 4.2	18.7 ± 5.6

TABLE II: The acceptances times efficiencies using the CDF phenomenological spectrum (CDF Sample) and MRSD$_0$ NLO (MRSD$_0$ Sample) MC simulation. The average $p_T(H_b)$ for the two spectra vary by no more than 1% in any transverse momentum bin.

$p_T(H_b)$ [GeV/c]	average $p_T(H_b)$ [GeV/c]	overall efficiency	
		CDF Sample	MRSD$_0$ Sample
9-11	9.9	1.47×10^{-3}	1.51×10^{-3}
11-13	11.9	6.12×10^{-3}	6.16×10^{-3}
13-17	14.8	1.38×10^{-2}	1.40×10^{-2}
17-23	19.6	2.68×10^{-2}	2.70×10^{-2}
23-29	25.5	3.90×10^{-2}	3.84×10^{-2}
29-40	33.2	4.61×10^{-2}	4.63×10^{-2}

TABLE III: The weights w_{ij} from the CDF phenomenological spectrum MC simulation with all momenta in GeV/c.

w_{ij}	$p_T(\mu^- D^0)$				
	9-11	11-13	13-17	17-29	29-40
$H_b \to DD, H_b \to D\tau$	5.54×10^{-2}	5.81×10^{-2}	5.94×10^{-2}	5.64×10^{-2}	1.84×10^{-2}
$p_T(H_b) < 9$	3.26×10^{-3}	$< 1 \times 10^{-6}$	$< 1 \times 10^{-6}$	$< 1 \times 10^{-6}$	$< 1 \times 10^{-6}$
9-11	3.02×10^{-1}	1.34×10^{-3}	$< 1 \times 10^{-6}$	$< 1 \times 10^{-6}$	$< 1 \times 10^{-6}$
11-13	3.78×10^{-1}	2.65×10^{-1}	1.00×10^{-4}	$< 1 \times 10^{-6}$	$< 1 \times 10^{-6}$
13-17	2.22×10^{-1}	5.27×10^{-1}	4.32×10^{-1}	5.77×10^{-4}	$< 1 \times 10^{-6}$
17-23	3.70×10^{-2}	1.31×10^{-1}	4.35×10^{-1}	3.73×10^{-1}	$< 1 \times 10^{-6}$
23-29	3.39×10^{-3}	1.51×10^{-2}	6.25×10^{-2}	3.59×10^{-1}	1.69×10^{-3}
29-40	6.00×10^{-5}	1.51×10^{-3}	1.04×10^{-2}	1.93×10^{-1}	6.35×10^{-1}
$p_T(H_b) > 40$	$< 1 \times 10^{-6}$	1.21×10^{-4}	3.83×10^{-4}	1.78×10^{-2}	3.45×10^{-1}

TABLE IV: The weights w_{ij} from the NDE+MRSD$_0$ MC simulation with all momenta in GeV/c.

w_{ij}	$p_T(\mu^- D^0)$ [GeV/c]				
	9-11	11-13	13-17	17-29	29-40
$H_b \to DD$, $H_b \to D\tau$	6.09×10^{-2}	6.26×10^{-2}	6.39×10^{-2}	6.50×10^{-2}	3.14×10^{-2}
$p_T(H_b) < 9\,\mathrm{GeV}/c$	2.06×10^{-3}	$< 1 \times 10^{-6}$	$< 1 \times 10^{-6}$	$< 1 \times 10^{-6}$	$< 1 \times 10^{-6}$
$9\text{-}11\,\mathrm{GeV}/c$	2.75×10^{-1}	1.38×10^{-3}	$< 1 \times 10^{-6}$	$< 1 \times 10^{-6}$	$< 1 \times 10^{-6}$
$11\text{-}13\,\mathrm{GeV}/c$	3.66×10^{-1}	2.42×10^{-1}	6.19×10^{-4}	$< 1 \times 10^{-6}$	$< 1 \times 10^{-6}$
$13\text{-}17\,\mathrm{GeV}/c$	2.43×10^{-1}	5.33×10^{-1}	3.88×10^{-1}	9.40×10^{-5}	$< 1 \times 10^{-6}$
$17\text{-}23\,\mathrm{GeV}/c$	4.98×10^{-2}	1.42×10^{-1}	4.66×10^{-1}	3.65×10^{-1}	$< 1 \times 10^{-6}$
$23\text{-}29\,\mathrm{GeV}/c$	3.29×10^{-3}	1.63×10^{-2}	6.82×10^{-2}	3.61×10^{-1}	1.21×10^{-3}
$29\text{-}40\,\mathrm{GeV}/c$	4.71×10^{-4}	2.28×10^{-3}	1.27×10^{-2}	1.91×10^{-1}	6.00×10^{-1}
$p_T(H_b) > 40\,\mathrm{GeV}/c$	$< 1 \times 10^{-6}$	7.90×10^{-5}	7.30×10^{-4}	1.76×10^{-2}	3.67×10^{-1}

TABLE V: The systematic uncertainties of the $d\sigma(p\overline{p} \to H_b)/dp_T$ measurement. All numbers listed in percent.

Source	p_T range [GeV/c]						
	All	9-11	11-13	13-17	17-23	23-29	29-40
Luminosity	6.0	6.0	6.0	6.0	6.0	6.0	6.0
L1 Efficiency	2.6	2.6	2.6	2.6	2.5	2.5	2.5
L2 XFT Efficiency	1.0	1.0	1.0	1.0	1.0	1.0	1.0
L2 SVT Efficiency	1.3	1.6	1.2	0.8	0.7	0.7	0.9
L3 Efficiency	0.2	0.2	0.2	0.2	0.2	0.1	0.1
CMU Efficiency	1.6	1.6	1.6	1.6	1.6	1.6	1.6
CMP Efficiency	$^{+1.4}_{-1.3}$	$^{+1.4}_{-1.3}$	$^{+1.4}_{-1.3}$	$^{+1.4}_{-1.3}$	1.4	1.5	1.7
SVX II Efficiency	$^{+1.5}_{-1.0}$	$^{+1.5}_{-1.0}$	$^{+1.5}_{-1.0}$	$^{+1.5}_{-1.0}$	$^{+1.5}_{-1.1}$	$^{+1.5}_{-1.1}$	$^{+1.5}_{-1.0}$
SVX II 2nd track Efficiency	1.0	1.0	1.0	1.0	1.0	1.0	1.0
COT Eff. (D^0)	$^{+3.1}_{-4.1}$	$^{+3.2}_{-4.3}$	$^{+3.3}_{-4.2}$	$^{+3.0}_{-3.8}$	$^{+2.9}_{-3.5}$	$^{+2.8}_{-3.3}$	$^{+2.7}_{-3.1}$
COT Eff. ($\mu^- D^{*+}$)	$^{+7.0}_{-8.9}$	$^{+7.9}_{-9.7}$	$^{+7.1}_{-9.6}$	$^{+6.1}_{-8.2}$	$^{+5.3}_{-6.1}$	$^{+4.9}_{-5.0}$	$^{+4.5}_{-4.3}$
Vertex + Fit Eff	0.4	0.4	0.4	0.4	0.4	0.4	0.4
$c\overline{c}$ Background	4.7	5.3	5.8	3.8	2.5	2.1	1.7
$b\overline{b}$ Background	0.6	0.6	0.6	0.6	0.6	0.6	0.6
d_0 Smearing	$^{+0.9}_{-2.6}$	$^{+1.1}_{-2.6}$	$^{+0.8}_{-2.8}$	$^{+0.7}_{-2.6}$	$^{+0.8}_{-2.3}$	$^{+1.0}_{-2.5}$	$^{+1.5}_{-1.4}$
final state radiation	1.2	1.0	1.8	1.8	0.7	2.2	4.0
$\mathcal{B}(H_b \to \mu^- D^{**}X)$ ($\mu^- D^0$)	1.9	2.1	1.7	1.6	2.0	1.5	1.7
$\mathcal{B}(H_b \to \mu^- D^{**}X)$ ($\mu^- D^{*+}$)	1.9	2.0	1.9	1.8	2.3	1.7	2.0
$\mathcal{B}(H_b \to DD)$, $\mathcal{B}(H_b \to D\tau)$	2.4	2.4	2.4	2.5	2.6	2.3	2.4
MC stat. ($\mu^- D^0$)	0.5	1.7	1.1	0.9	1.0	1.6	2.1
MC stat. ($\mu^- D^{*+}$)	1.2	5.8	3.4	2.2	2.2	3.3	4.4
MC p_T shape ($\mu^- D^0$)	3.4	5.7	3.0	1.7	2.2	2.0	2.5
MC p_T shape ($\mu^- D^{*+}$)	4.4	5.7	4.4	3.9	4.0	0.6	2.8
Total ($\mu^- D^0$)	$^{+10.4}_{-11.0}$	$^{+11.9}_{-12.4}$	$^{+11.0}_{-11.5}$	$^{+9.6}_{-10.1}$	$^{+9.2}_{-9.6}$	$^{+9.2}_{-9.6}$	$^{+10.0}_{-10.1}$
Total ($\mu^- D^{*+}$)	$^{+12.5}_{-13.9}$	$^{+14.9}_{-16.0}$	$^{+13.5}_{-15.1}$	$^{+11.7}_{-13.1}$	$^{+11.0}_{-11.5}$	$^{+10.3}_{-10.5}$	$^{+11.5}_{-11.3}$

TABLE VI: Differential cross section $d\sigma(p\overline{p} \to H_b)/dp_T$ and differential cross section times branching fraction of $H_b \to \mu^- D^0 X$, $D^0 \to K^- \pi^+$ where the first uncertainty is statistical and the second is systematic. In the case of the differential cross section, the third uncertainty arises from the applied branching fractions.

p_T bin [GeV/c]	$d\sigma/dp_T \times \mathcal{B}$ [pb/(GeV/c)]	$d\sigma/dp_T$ [pb/(GeV/c)]
9-11	$762 \pm 50^{+91}_{-94}$	$287 \pm 19^{+34}_{-35} \pm 15$
11-13	$403 \pm 18^{+44}_{-44}$	$152 \pm 7 \pm 17 \pm 8$
13-17	$179 \pm 6^{+17}_{-18}$	$67.3 \pm 2.3^{+6.4}_{-6.8} \pm 3.6$
17-23	$49.7 \pm 1.5^{+4.6}_{-4.8}$	$17.8 \pm 0.6^{+1.7}_{-1.8} \pm 0.9$
23-29	$13.1 \pm 0.6^{+1.2}_{-1.3}$	$4.93 \pm 0.23^{+0.45}_{-0.49} \pm 0.26$
29-40	$3.43 \pm 0.20^{+0.34}_{-0.35}$	$1.29 \pm 0.08 \pm 0.13 \pm 0.07$

TABLE VII: Differential cross section $d\sigma(p\overline{p} \to H_b)/dp_T$ and differential cross section times branching fraction of $H_b \to \mu^- D^{*+} X$, $D^{*+} \to D^0 \pi^+$, $D^0 \to K^- \pi^+$ where the first uncertainty is statistical and the second is systematic. In the case of the differential cross section, the third uncertainty arises from the applied branching fractions.

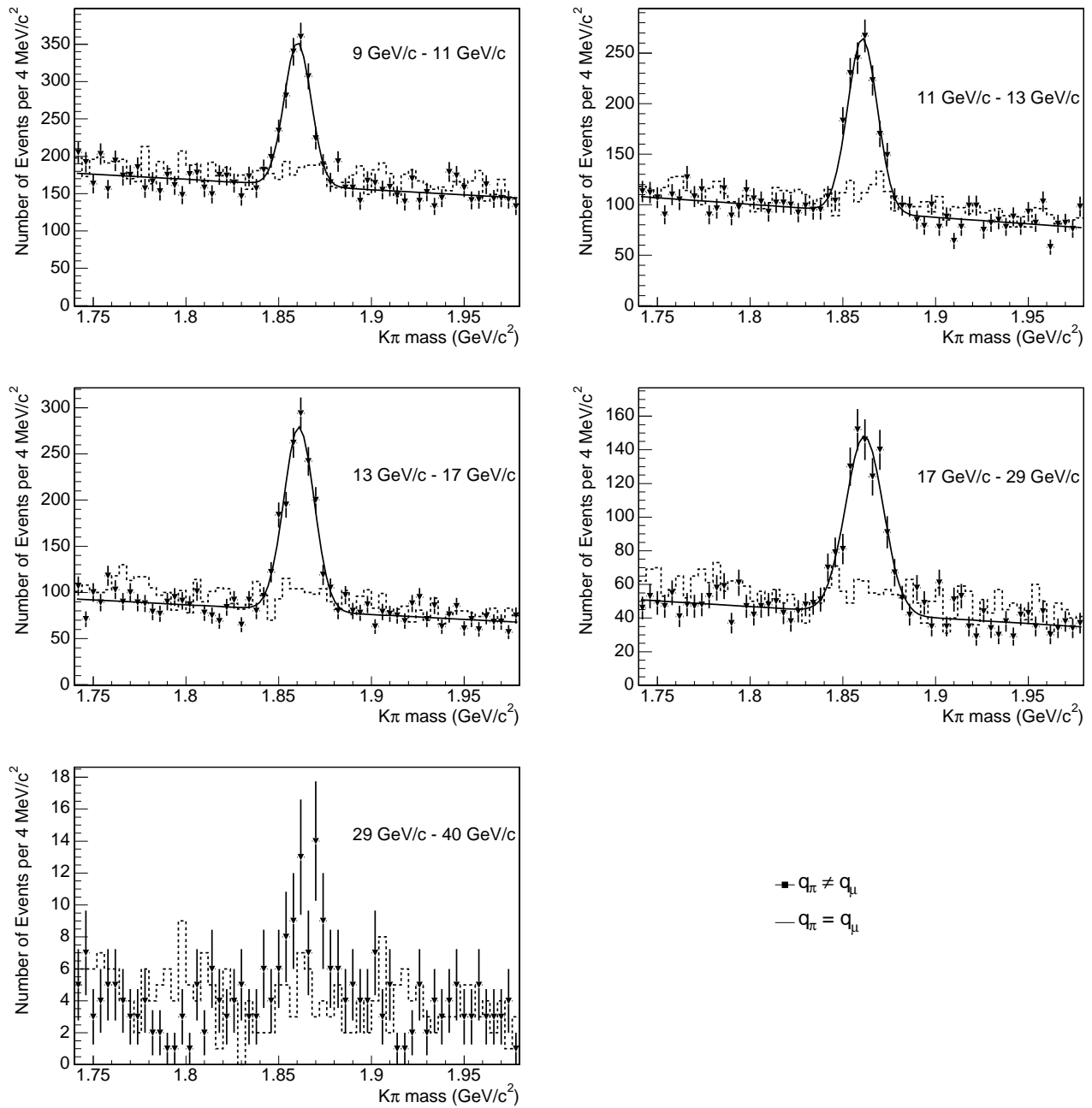| p_T bin [GeV/c]	$d\sigma/dp_T \times \mathcal{B}$ [pb/(GeV/c)]	$d\sigma/dp_T$ [pb/(GeV/c)]
9-11	$226 \pm 30^{+34}_{-36}$	$312 \pm 41^{+47}_{-50} \pm 22$
11-13	$122 \pm 10^{+16}_{-18}$	$168 \pm 14^{+22}_{-25} \pm 12$
13-17	$56.0 \pm 3.0^{+6.5}_{-7.3}$	$77.3 \pm 4.1^{+9.0}_{-10.1} \pm 5.5$
17-23	$15.4 \pm 0.7^{+1.7}_{-1.8}$	$21.3 \pm 1.0^{+2.3}_{-2.5} \pm 1.5$
23-29	$3.84 \pm 0.25^{+0.40}_{-0.40}$	$5.30 \pm 0.35 \pm 0.55 \pm 0.37$
29-40	$0.95 \pm 0.09^{+0.11}_{-0.11}$	$1.31 \pm 0.12 \pm 0.15 \pm 0.09$

FIG. 1: The π^+K^- mass for different ranges of $p_T(\mu^-K^-\pi^+)$. Points indicate events where the muon and pion have opposite charges, which is the right sign correlation, and the dashed histograms contain events where the muon and pion have the same charge, which is the wrong-sign correlation. The solid line is a fit to 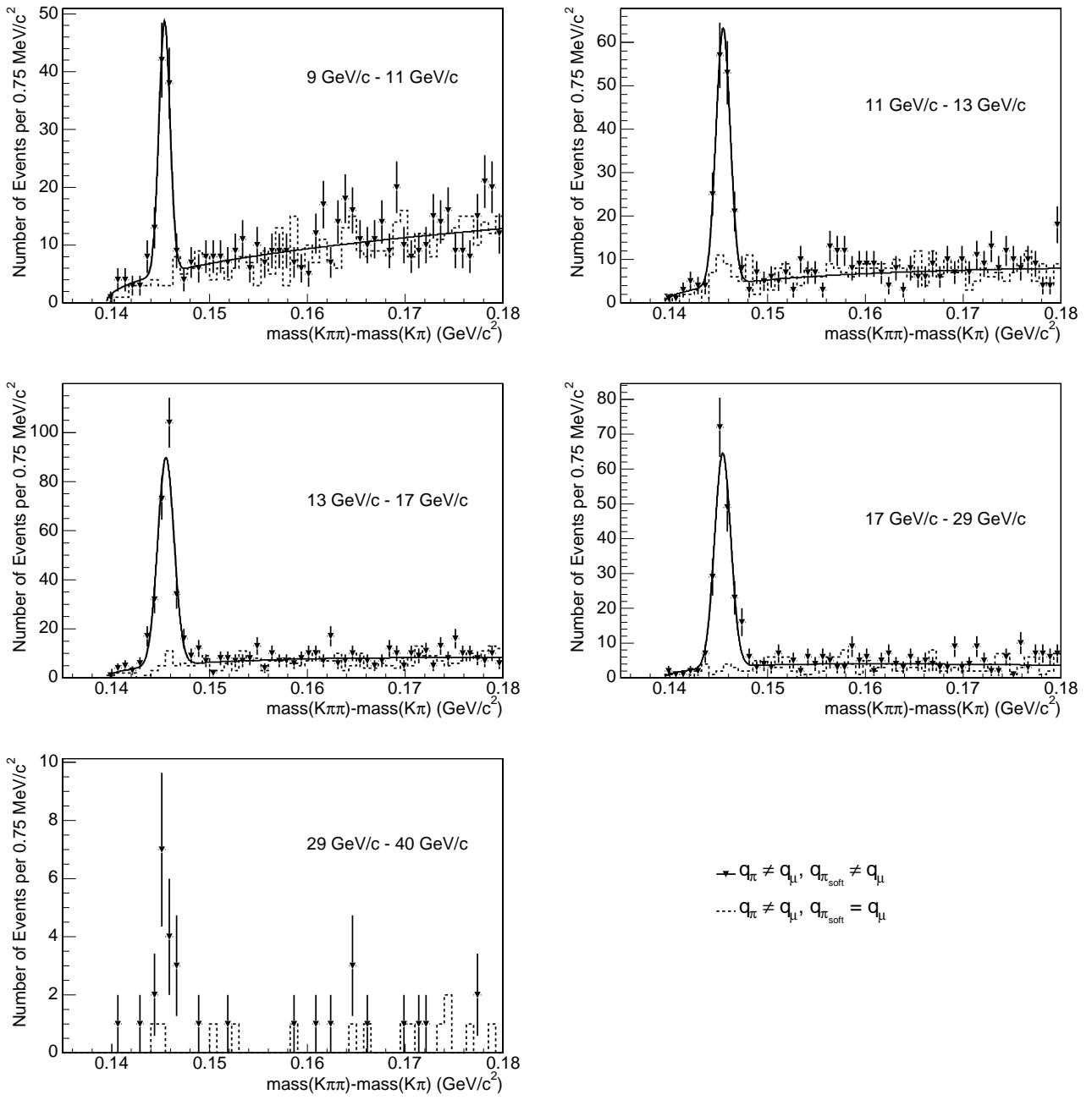the right sign data using a gaussian plus linear background. The χ^2 per degree of freedom for these fits range from 0.9 to 1.2. Due to low statistics, the yield in the highest p_T bin is measured by sideband subtraction.
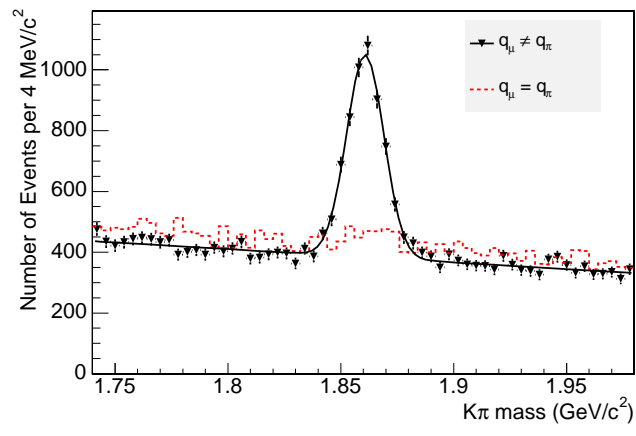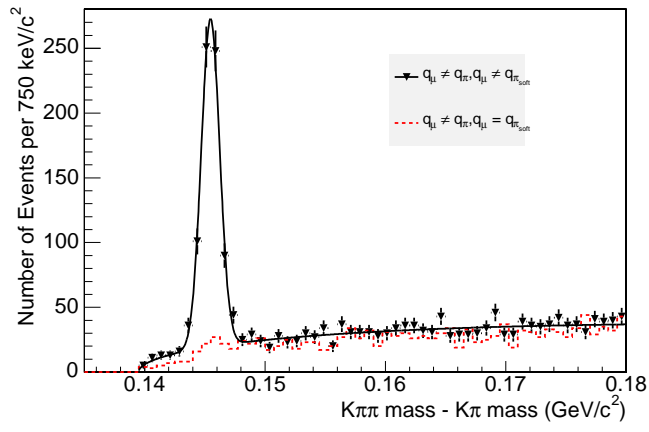
FIG. 2: The $\pi^+ K^-$ mass for $p_T(\mu^- K^- \pi^+) > 9.0$ GeV/c. The solid histogram shows events with the right sign correlation between muon and pion, and the dashed histogram shows events where the muon and pion have the wrong-sign correlation. The solid line is a fit to the right sign data using a gaussian plus linear background.

FIG. 3: The mass difference between $\pi_{soft}\pi^+K^-$ and π^+K^- for different ranges of $p_T(\mu^-K^-\pi^+)$. All events shown are selected such that the muon and the pion from the candidate D^0 have opposite charge. Points show events where the muon and soft pion have opposite charge, which is the right sign correlation, and the dashed histograms represent events where the muon and soft pion have the same charge, which is the wrong-sign correlation. The χ^2 per degree of freedom for these fits ranges from 1.1 to 1.3. Due to low statistics, the yield in the highest p_T bin is measured by sideband subtraction.

FIG. 4: Distribution of the difference between the $\pi^+_{soft}\pi^+K^-$ and the π^+K^- invariant masses for $p_T(\mu^-K^-\pi^+) > 9.0$ GeV/c. The solid histogram indicate events with the right sign correlation between muon and pion, and the dashed histogram contain events where the muon and pion have the wrong-sign correlation.
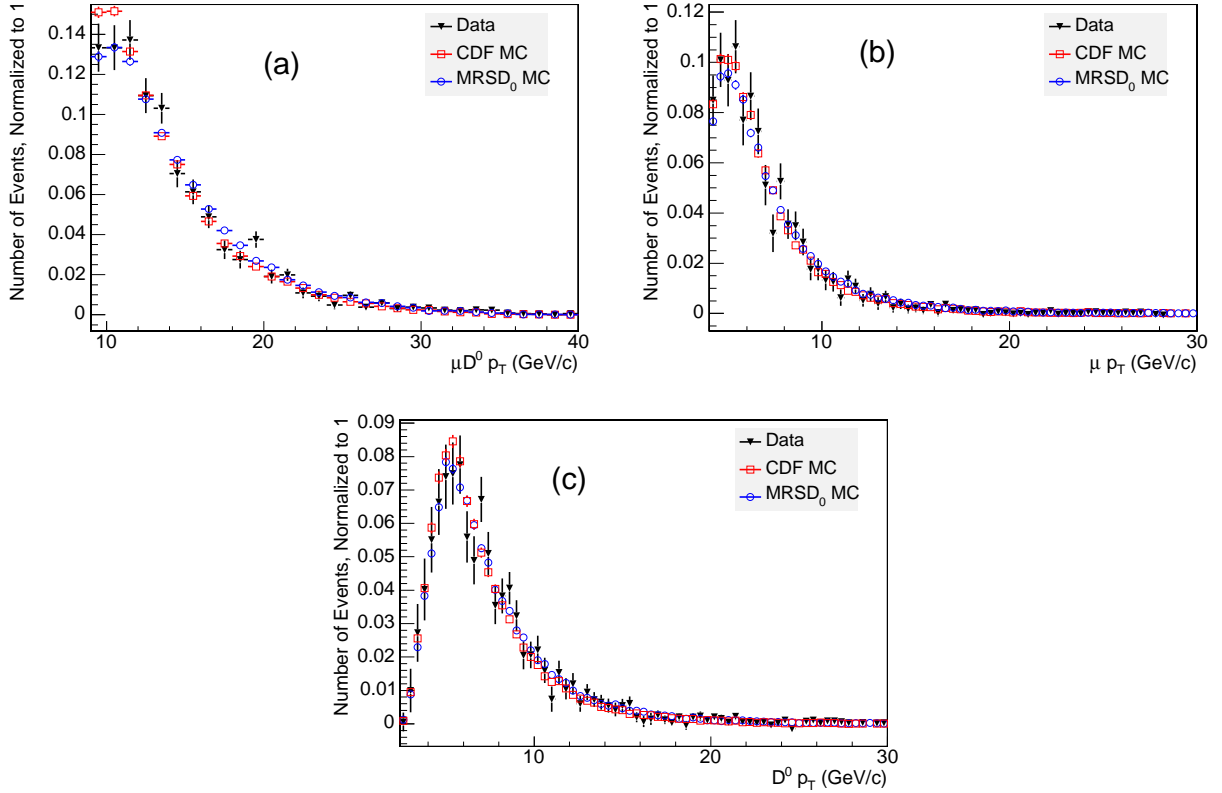
FIG. 5: A comparison of the two MC simulated samples to data, plotted as a function of the p_T of (a) the μ^-D^0, (b) the μ, and (c) the D^0. The data is seen to have a higher $p_T(\mu^-D^0)$ than the CDF MC sample, while the data is seen to have a lower $p_T(\mu^-D^0)$ than the MRSD$_0$ NLO MC simulation.
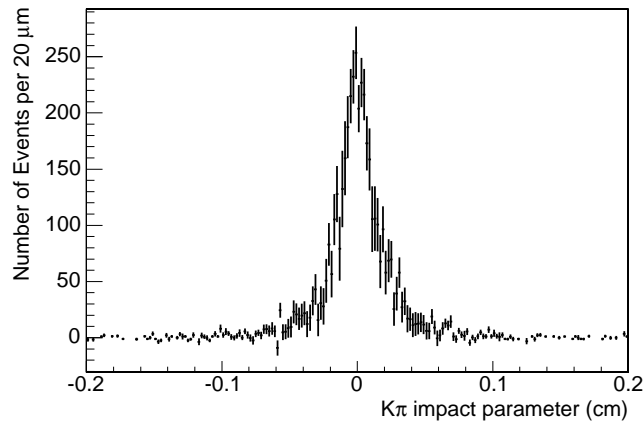
FIG. 6: The D^0 impact parameter distribution for the data after sideband subtraction.
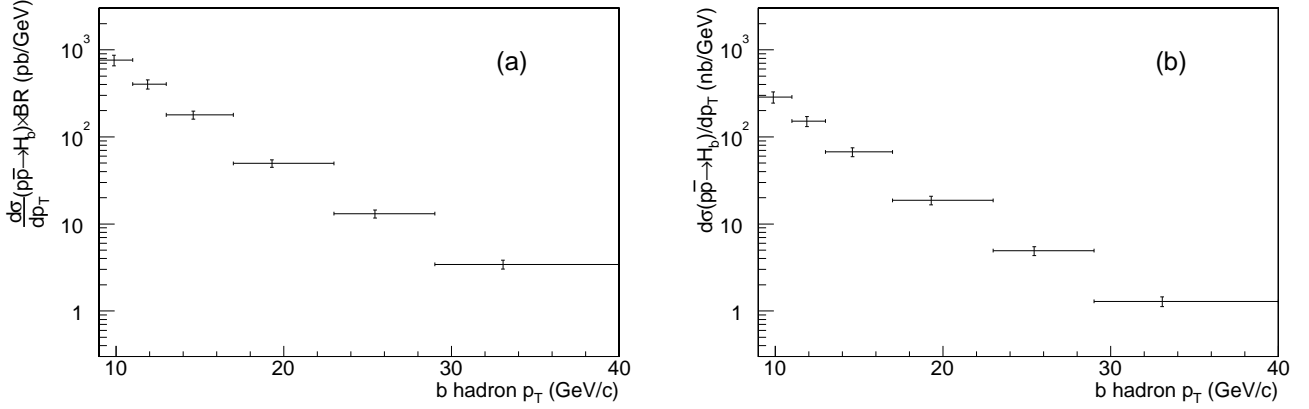
FIG. 7: The differential cross section times branching ratio for $H_b \rightarrow \mu^- D^0 X$, $D^0 \rightarrow K^- \pi^+$ is shown on the left, where BR is shorthand notation for the product of branching ratios, $BR = \mathcal{B}(H_b \rightarrow \mu^- D^0 X) \times \mathcal{B}(D^0 \rightarrow K^- \pi^+)$. The uncertainties shown on each point include statistical and systematic uncertainties combined in quadrature. Incorporating measured branching ratios [30], the differential cross section is shown on the right. The uncertainties on each point include statistical, systematic and branching ratio uncertainties added in quadrature.
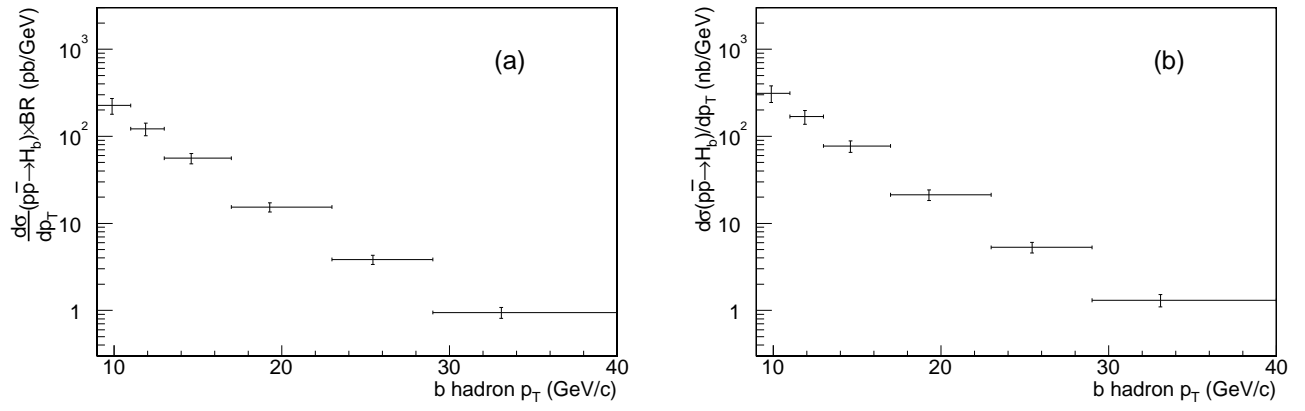
FIG. 8: The differential cross section times branching ratio for $H_b \to \mu^- D^{*+} X$, $D^{*+} \to D^0 \pi^+_{soft}$, $D^0 \to K^- \pi^+$ is shown on the left, where BR is shorthand notation for the product of branching ratios, $BR = \mathcal{B}(H_b \to \mu^- D^0 X) \times \mathcal{B}(D^0 \to K^- \pi^+) \times \mathcal{B}(D^{*+} \to D^0 \pi^+)$. The uncertainties shown on each point include statistical and systematic uncertainties combined in quadrature. Incorporating measured branching ratios [30], the differential cross section is shown on the right. The uncertainties on each point include statistical, systematic and branching ratio uncertainties added in quadrature.
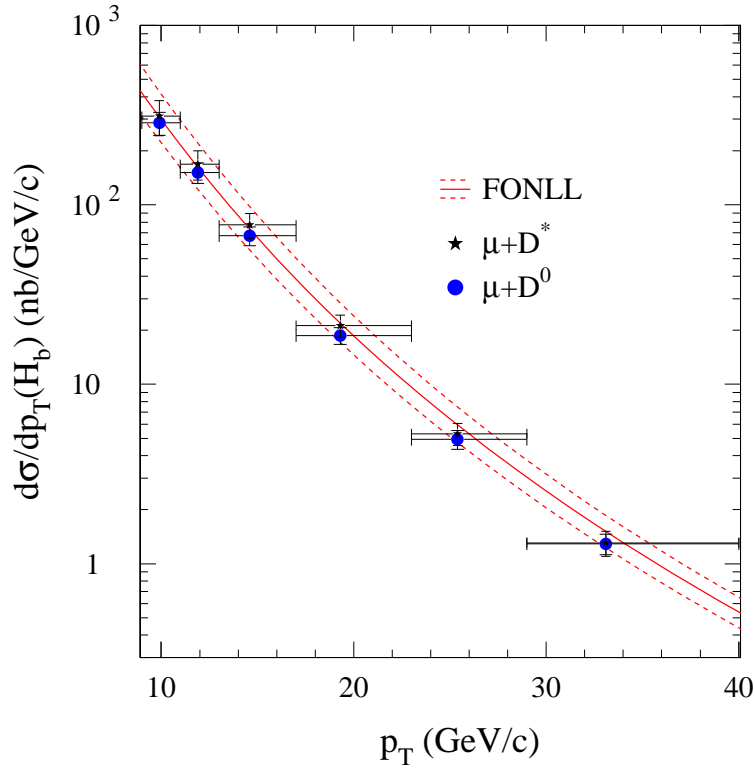

FIG. 9: The b-hadron differential cross section for $|y(H_b)| < 0.6$ from FONLL theory [10] compared with measurements from $H_b \to \mu^- D^0 X$ ($D^0 \to K^- \pi^+$) and $H_b \to \mu^- D^{*+} X$ ($D^{*+} \to D^0 \pi^+_{soft}$ and $D^0 \to K^- \pi^+$).
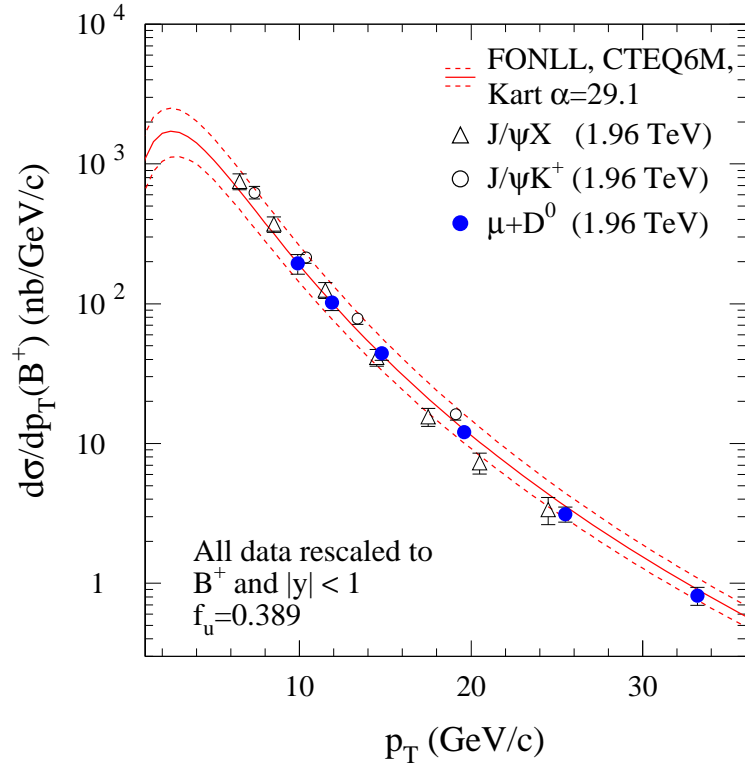
FIG. 10: Comparison of differential b cross section results. The results presented are $H_b \to J/\psi X$ at $\sqrt{s} = 1.96\,\text{TeV}$ [8], $B^+ \to J/\psi K^+$ at $\sqrt{s} = 1.96\,\text{TeV}$ [12], and this result for $H_b \to \mu^- D^0 X$ at $\sqrt{s} = 1.96\,\text{TeV}$. All results are scaled to $|\eta| < 1$. For comparison, the FONLL [10] calculation is included.